8-2011

EVLA imaging of methanimine and hydrogen cyanide in Arp 220

Matthew R. Rickert
DePaul University, MRICKER@LUC.EDU

Follow this and additional works at: https://via.library.depaul.edu/etd

Recommended Citation

EVLA IMAGING OF METHANIMINE AND HYDROGEN CYANIDE IN ARP 220

A Thesis

Presented in

Partial Fulfillment of the

Requirements for the Degree of

MASTER OF SCIENCE

August, 2 0 1 1

BY

Matthew Rickert

PHYSICS DEPARTMENT

College of Liberal Arts and Sciences

DePaul University

Chicago, Illinois

TABLE OF CONTENTS

LIST OF FIGURES

LIST OF TABLES

ACKNOWLEDGEMENTS

ABSTRACT

We present observations of the 5289.8 MHz $1_{10} \rightarrow 1_{11}$ transition of the pre-biotic molecule methanimine (H_2CNH) and the 6731.9 MHz J=5 direct l-type transition in the vibrationally excited ($\nu_2 = 1$) state of hydrogen cyanide (HCN) toward the nearest Ultraluminous Infrared Galaxy, Arp 220, taken with the Expanded Very Large Array (EVLA) in A configuration. The 5289.8 MHz H_2CNH line was detected in emission toward the western nucleus, but not toward the eastern nucleus. The 6731.9 MHz HCN line was detected in absorption toward the western nucleus, but not toward the eastern nucleus. Both of these are new results from the observations reported in this thesis, and are in contrast with rotational HCN transitions that trace cold and dense molecular gas and have been observed in emission toward both nuclei. We have also confirmed that the H_2CNH line is most likely a maser; this represents the first independent confirmation of the only H_2CNH maser ever detected. This H_2CNH maser was found to have an isotropic luminosity of 5 $L_\odot$, close to the luminosity (12 $L_\odot$) of a formaldehyde maser in Arp 220, and similar to the luminosities of H_2O kilomasers, most of which are believed to be excited in active star forming regions in external galaxies. The western nucleus is known to have undergone an intense starburst, and we conclude that the H_2CNH maser is being amplified in the foreground gas along the line of sight to the western nucleus by the background continuum of the nucleus. The absorbing HCN gas toward the western nucleus was found to have a column density $\sim 1.04 \times 10^{19}$ cm^{-2} corresponding to an excitation temperature near 550 K; the column density may be an order of magnitude higher at $\sim 10^{20}$ cm^{-2} if the excitation temperature has a lower value of 150 K. If we assume that the HCN abundance relative to molecular hydrogen is the same as in our Galaxy (10^{-5}), this gives about 1×10^{24} cm^{-2} (or 10^{25} cm^{-2}) for the molecular hydrogen column density, which is in reasonable agreement with the values reported by other observers toward the western nucleus. We conclude that the observed HCN absorption is likely taking place in a column of highly

excited molecular gas in the foreground of the western nucleus. The observations reported in this thesis provide a self consistent picture of highly excited gas in the foreground of the western nucleus, and a convincing demonstration that the line of sight toward the western nucleus has different physical conditions than that toward the eastern nucleus. These observations have demonstrated conclusively that a new range of molecular transitions can now be detected and imaged with cm-wavelength telescopes like the EVLA, thus opening up new opportunities for the study of the physics and chemistry of other galaxies.

CHAPTER 1

Introduction

This work is solely based on spectroscopic measurements. The dictionary defines spectroscopy as "the branch of science concerned with the investigation and measurement of spectra produced when matter interacts with or emits electromagnetic radiation." This allows information to be gleaned about the matter based solely on the observed radiation. It should be of no surprise, therefore, that spectroscopy is widely used in astronomy, as the only way it is possible to learn anything outside of our solar system is through observations of the radiation that reaches Earth. A key use of spectroscopy is the ability to identify specific molecular transitions. This can immediately identify the presence of a specific molecule in the region from which the radiation was emitted or where it was absorbed. In turn, this can provide further information on the physical structure and chemistry of the region where that molecule is present, as the transitions can only occur under specific conditions.

In this thesis we present observations of two spectral transitions: the 6731.9 MHz J=5 direct l-type transition in the vibrationally excited ($\nu_2 = 1$) state of hydrogen cyanide (HCN) and the 5289.8 MHz $1_{10} \rightarrow 1_{11}$ transition of methanimine (H_2CNH) in the galaxy Arp 220 using the Expanded Very Large Array (EVLA). Arp 220 is the nearest Ultraluminous Infrared Galaxy (ULIRG), meaning that it has an infrared luminosity greater than 10^{12} $L_\odot$. Such ULIRGs are believed to be powered by either an extensive burst of star formation in the nuclear region (called a starburst) or an active galactic nucleus (AGN), or both. Understanding the physical processes and chemistry of nearby ULIRGs like Arp 220 has become even more important after the discovery of young counterparts of ULIRGs at high redshifts (Ivison et al. 2000). Such high redshift galaxies are usually heavily obscured by dust, have small angular sizes, and low intensity. Therefore, observations of Arp 220 allow us to understand the impact of star formation and AGN activity in its high redshift counterparts.

The observations in this thesis constitute an important milestone on the road to a better understanding of Arp 220, but are not intended to address whether Arp 220 is powered by starbursts or an active galactic nucleus (AGN). In order to set the context and provide the necessary background to understand these observations, we provide an introduction to astronomical spectroscopy in Section 1.1, discuss the use of interferometry in astronomical measurements in Section 1.2, the structure and properties of the observed galaxy Arp 220 in Section 1.3, and the prebiotic molecules H_2CNH and HCN in Section 1.4. In Chapter 2 we discuss the observations and the data reduction. Chapter 3 contains our results and a discussion of those results. Finally, Chapter 4 summarizes our conclusions and describes future work to be conducted on this subject.

1.1 Introduction to Spectroscopy

When a molecule becomes energized due to some interaction (such as colliding with other matter or absorbing a photon), it will ultimately revert back to a less energized state by emitting radiation at a specific frequency. Figure 1.1 (top) shows an example of such an emission line; in it the intensity of the emission has been plotted along the vertical axis, while the heliocentric velocity (described in more detail at the end of this section) of the line has been plotted along the horizontal axis. Additionally, it is possible for the molecular transition to be observed as an absorption, where background electromagnetic radiation is absorbed by the molecule, causing it to become excited, thus causing a dip in the background continuum (Figure 1.1, bottom). Fortunately, through laboratory work, the frequencies of many different transitions have already been measured, and it has been determined that the different transitions have different unique frequencies that are produced. This means that if a certain frequency is observed from an astronomical source, that frequency can be compared to previously cataloged frequencies, and if a match is found, the astronomer is able to identify what molecular transition is occurring in the observed astronomical source. By knowing the molecular transition occurring in the source,
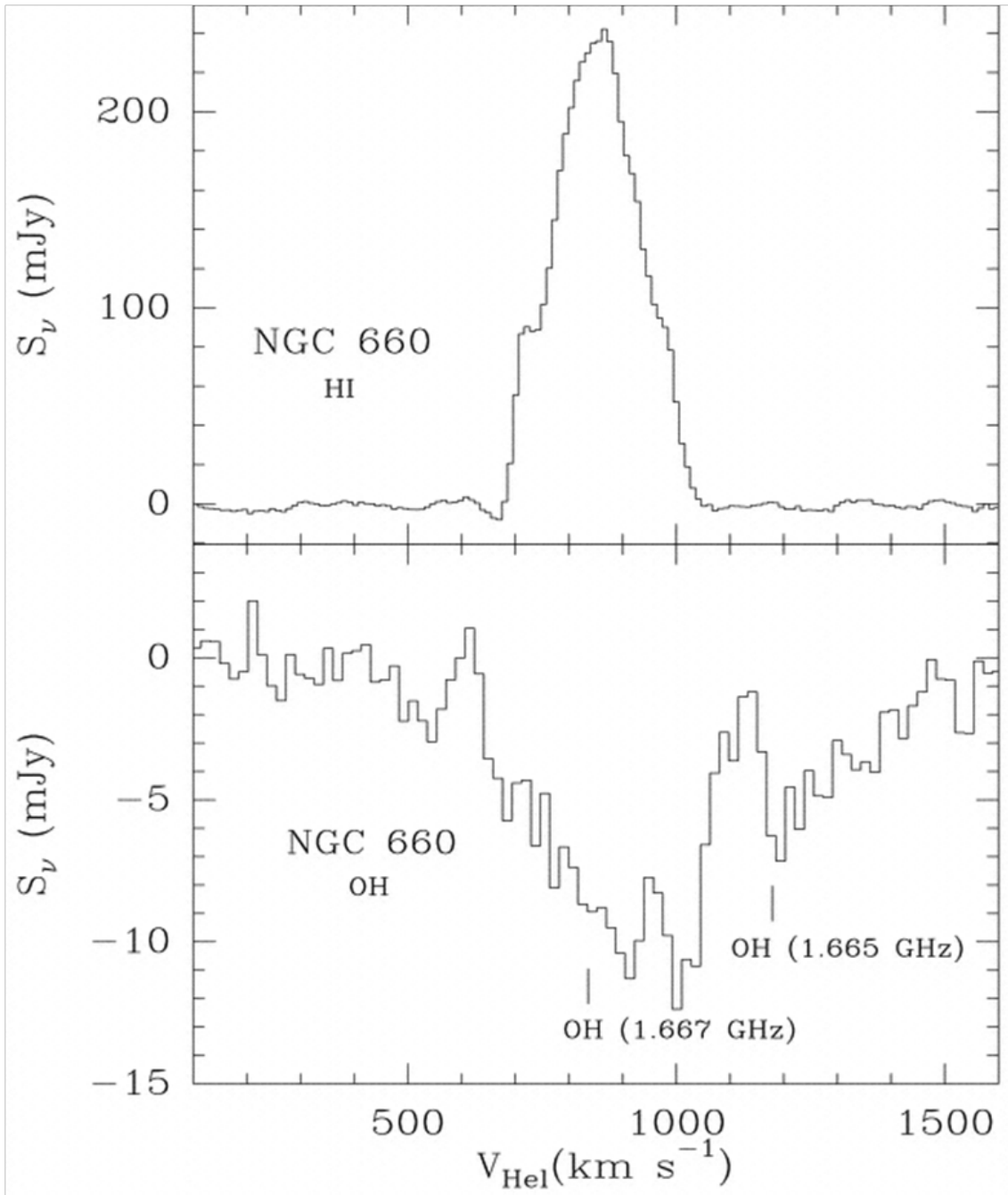
Figure 1.1: Example of spectral lines from the polar ring galaxy NGC 660 (Araya et al. 2004). Top: An example of a spectral emission line for HI. Bottom: An example of a spectral absorption line for OH (note that there are two absorption lines: 1.667 GHz & 1.665 GHz). The vertical axis gives the flux density (S_ν), while the horizontal axis shows the velocity with respect to our Sun (v_{Hel}), as is the convention for observations of extragalactic objects.

the astronomer can gain some understanding of the conditions that must be present in that source. This is because certain molecules can only occur in certain environments (e.g. a specific temperature range), and the specific molecular transition can only occur under certain conditions as well (e.g. appropriate excitation conditions). Finally, the astronomer can learn about the physical structure and the movement of the source by determining if the observed frequency is either higher or lower than the laboratory frequency due to the Doppler shift. This would occur if the the astronomical source is moving toward or away from the observer, as per the equation for Doppler shift:

$$f = \sqrt{\frac{c + u}{c - u}} f_0, \tag{1.1}$$

where f is the observed frequency, f_0 is the laboratory frequency, u is the velocity of the source, and c is the speed of light. This can be particularly useful for extended bodies, where part of the source may be moving towards the observer, while another part of the source may be moving away, as in the case of rotational motion of an extended body whose axis of rotation is not parallel to the observer's line of sight. Thus observations of the Doppler shift can provide insight into the internal dynamics of an extended source. Finally, Equation 1.1 is used to convert between the observed frequency and the heliocentric velocity. The heliocentric velocity is the velocity of the observed source (u in Equation 1.1) with respect to the sun that results in the frequency that is observed (f in Equation 1.1).

1.2 Radio Interferometry

Molecular transitions involve discrete energy levels, and therefore can only be detected at specific frequencies. For example, rotational transitions (described later in Section 1.4.2) have lower energy differences and therefore are seen solely at radio frequencies. Moreover, radio waves are able to pass through the gas and dust found in the interstellar medium and at the center of galaxies due to their long wavelengths. Therefore, radio waves are ideal for probing the nuclei of galaxies, such as Arp 220,

which are highly enshrouded by dust. However, the long wavelengths also create a difficulty in the form of poor angular resolution. The angular/spatial resolution (R) of a telescope is proportional to the wavelength (λ) being observed, divided by the diameter (D) of the aperture,

$$R \approx \frac{\lambda}{D} \tag{1.2}$$

For radio astronomy the wavelength can be rather large (with wavelengths of up to 100 m), requiring a much larger aperture in order to obtain similar resolutions to that obtained in other branches of astronomy. The Arecibo telescope, which is the largest telescope in the world (Figure 1.2), has a diameter of 305 m and an angular resolution between $0.5'$ (X-Band, 12–18 GHz) and $3.5'$ (L-Band, 1–2 GHz), while a 15 cm optical telescope would have an angular resolution of $\sim 0.0092''$. As building even larger telescopes present certain logistical impossibilities, interferometry is utilized in order to generate better resolution without the need of excessively larger telescopes. Interferometry is the process of obtaining information through the interference of electromagnetic waves. In order to use interferometry for astronomical observation, at least two telescopes (or antennas in the case of radio astronomy) are required. The telescopes are separated by a baseline $\vec{b}$, and for a signal coming along $\hat{s}$ at a speed c a geometric time delay (τ_g) of $\vec{b} \cdot \hat{s}/c$ would be introduced into the signal received by one of the antennas (and therefore, the actual voltage produced by the antenna, V_1, would also contain the time delay, see Figure 1.3). In the case of astronomical interferometers like the EVLA (Figure 1.4), the voltage is digitized at the antennas and then sent to the correlator. The correlator is a device that multiplies and averages the signals from the different antennas, as well as integrating over the solid angle ($d\Omega$), as most sources are extended sources. In the case of the EVLA, the correlator is a computer that digitally performs these actions. The correlator then produces the complex visibility (V_ν) for the given observed frequency (ν):

$$V_\nu(\vec{b}) = \int \int I_\nu(\hat{s}) e^{-i(2\pi\nu \frac{\vec{b} \cdot \hat{s}}{c})} d\Omega, \tag{1.3}$$

Figure 1.2: Photograph of the single dish Arecibo radio telescope (courtesy of the NAIC – Arecibo Observatory, a facility of the NSF). The Arecibo radio telescope is the largest single aperture telescope in the world, located in a basin in Puerto Rico with a diameter of 305 m (notice the cars in the lower right corner to appreciate the scale). Despite this large aperture size, due to the large wavelengths of radio waves, Arecibo still has a fairly poor resolution (0.5′ in X-Band 12–18 GHz to 3.5′ in L-Band 1–2 GHz), making it a poor imaging instrument. The large collecting area does make it an ideal survey instrument, as Arecibo is then able to observe large portions of the sky in a small amount of time.
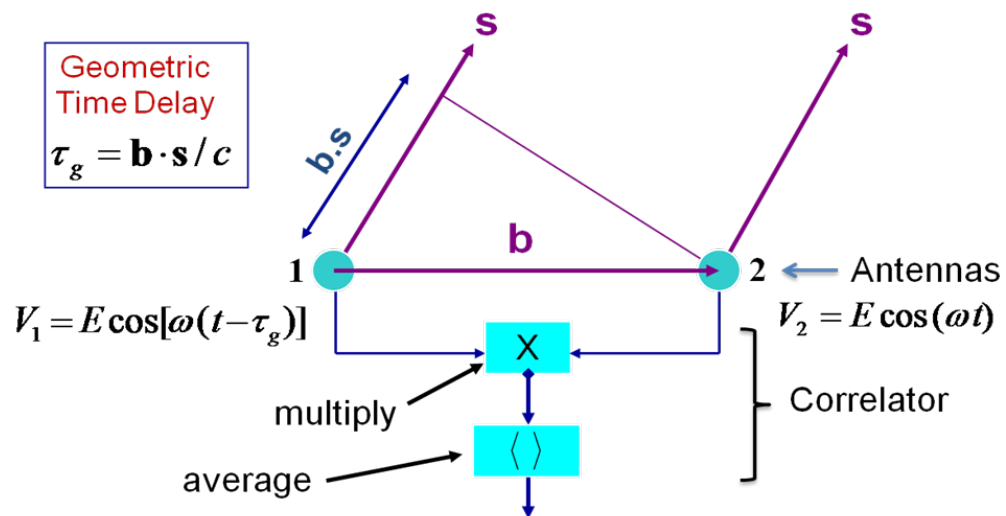
Figure 1.3: Diagram of an interferometer set up using two antennas (1,2) separated by $\vec{b}$ with an incoming signal along $\hat{s}$. Due to the separation between the antennas, a geometric time delay τ_g of $\vec{b} \cdot \hat{s}/c$ is introduced to the signal received by antenna 1. These signals are then converted into a voltage produced by each antenna (V_1, V_2), with V_1 similarly containing the time delay. The voltages from the antennas are then digitized, and sent to the correlator, where they are multiplied and averaged together (Perley 2010).

Figure 1.4: Photograph of the EVLA, located in New Mexico (courtesy of the NRAO – a facility of the NSF operated under cooperative agreement by Associated Universities Inc.). Each individual EVLA antenna has a diameter of 25 m, which is much smaller than the diameter of the Arecibo single dish (305 m). Using the technique of interferometry (described in Section 1.2), signals received by the EVLA antennas can be combined so that the array performs like a single telescope with an equivalent dish diameter equal to the maximum distance between the antennas. The telescopes are mounted on railroad tracks to allow the spacing to be modified into four different configurations or arrays. In the picture the EVLA is in D configuration where the antennas are as close together as possible. Being able to change the distance between antennas allows the resolution to be adjusted, and in A configuration (when the antennas are separated by the most distance) the EVLA has a much better resolution than Arecibo (0.24″ in X-Band to 1.4″ in L-Band, see Section 2.1 for more information on the EVLA).
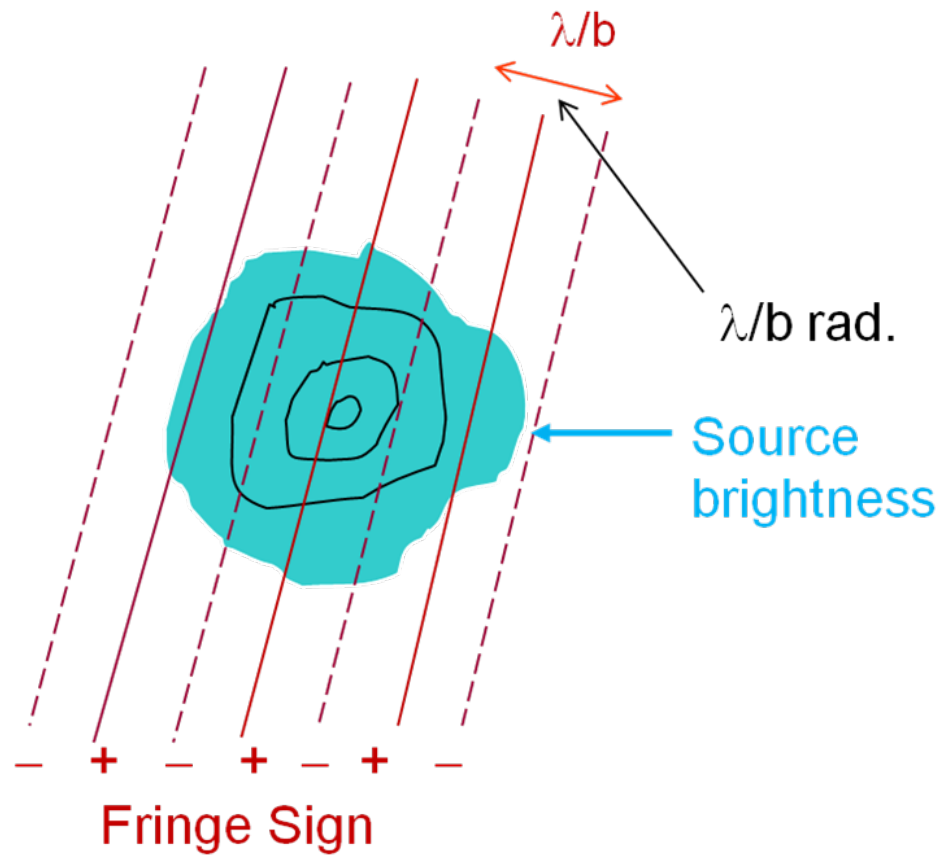
Figure 1.5: Diagram of how the correlator can be considered to be projecting sinusoidal fringes over an extended astronomical source, with wavelength λ/b (where λ refers to the observation wavelength, and b is the baseline length). The crests (+) of the the sinusoidal function are represented by solid lines, while the troughs (−) are represented by dashed lines. The varying intensity of the source (represented by the contours) can then be considered to be multiplied with the overlaid sinusoidal pattern by the correlator (Perley 2010). A larger baseline would therefore result in a smaller wavelength for the fringe pattern, which would correspond to a better resolution.

$I_\nu(\hat{s})$ is the intensity of the source along $\hat{s}$. Through the simple trigonometry identity $e^{ix} = \cos x + i \sin x$, it can be seen that the complex visibility is the source intensity multiplied by a complex sinusoidal function and integrated over the solid angle. The correlator can then be thought of as projecting a sinusoidal fringe pattern across the sky, which is then multiplied by the intensity of the extended source (Figure 1.5). From Equation 1.3 the wavelength of the fringe pattern can be determined through trigonometry to be λ/b, which demonstrates that a larger baseline will result in a smaller fringe wavelength and therefore a greater resolution. Thus the complex visibility allows for an observation of a source where the angular resolution is based on the distance between antennas and not the size of the antennas themselves, thus eliminating the need to create larger antennas in order to improve the angular resolution. In general, most astronomical interferometers (such as the EVLA) are composed of an array of antennas (more than just two) to ensure a better coverage of the sky and to reduce the amount of observing time required.

1.3   Arp 220

Arp 220 (IC 4533) is a galaxy located at Right Ascension $= 15^{\rm h}$ $34^{\rm m}$ $57.1^{\rm s}$, and Declination $= +23° \, 30' \, 11''$ (J2000 coordinates), at a redshift $z = 0.018126$ corresponding to a distance of ~ 77 Mpc (assuming $H_0 = 70$ km s^{-1} Mpc^{-1})[1]. Arp 220 has generated sustained interest since the 1980's, after observations with the IRAS satellite revealed that it has an extremely high infrared luminosity of 1.4×10^{12} $L_\odot$ (Soifer et al. 1987), where the solar luminosity, $L_\odot = 3.826 \times 10^{26}$ W. It soon became the nearest example of a class of objects called Ultra Luminous Infrared Galaxies (ULIRGs). ULIRGs are by definition galaxies with $L_{IR} > 10^{12} L_\odot$. Arp 220 contains numerous starbursts (Rovilos et al. 2003) and supernovae (Lonsdale et al. 2006). It also has an OH megamaser (Diamond et al. 1989); OH megamasers occur in ULIRGs and are extremely strong masers (see Section 1.4.3) with

---

[1]This is based on Hubble's Law: $v = H_0 D$, where v is the velocity of the object, H_0 is the Hubble "constant," D is the distance, and the definition of redshift (z): $(1+z)^2 = (c+v)/(c-v)$.

an isotropic luminosity greater than $10^3 L_\odot$ (Darling 2005), i.e., more than a million times brighter than OH masers in our own Galaxy. All these phenomena are the result of a cataclysmic event in Arp 220's past; Arp 220 is believed to be a galactic merger composed of the remnants of two colliding spiral galaxies (Mundell et al. 2001). In Section 1.3.1 below, we describe the structure of Arp 220 in more detail, and in Section 1.3.2, we discuss the blind spectral survey with the Arecibo telescope that led to the work in this thesis.

1.3.1 Structure

Since ULIRGs are usually heavily obscured by dust, not much is revealed by optical images of Arp 220 beyond its classification as a peculiar galaxy due to the presence of tidal tails (e.g. Figure 1.6). At near infrared and radio wavelengths, Arp 220 is observed to contain two nuclei (Figure 1.7, Scoville et al. 1998). The two nuclei are separated by 466 pc; the western nucleus is 204 pc in diameter, whereas the eastern nucleus has a diameter of 334 pc (Baan & Haschick 1995). From H I observations, the dynamical mass of the western nucleus has been found to be $1.1 \times 10^9 M_\odot$, whereas that of the eastern nucleus has been found to be $1.7 \times 10^8 M_\odot$ (Mundell et al. 2001). The two nuclei orbit each other with an orbital period of 7×10^6 yr (Baan & Haschick 1995). The western nucleus also rotates in the same direction as its orbital motion about the eastern nucleus (i.e., prograde), whereas the eastern nucleus rotates in the opposite direction (Mundell et al. 2001). A schematic of the geometry and rotational motions is shown in Figure 1.8. Most of the molecular gas in the galaxy ($\sim 10^9 M_\odot$) is confined in a thin disk of diameter 1 kpc (Scoville et al. 1991) which is coplanar with, and rotates in the same direction as, the eastern nucleus.

1.3.2 Arecibo Spectral Survey of Arp 220

The observations reported in this thesis were prompted by a blind spectral survey of Arp 220 conducted by Arecibo in 2008. In a blind spectral survey, a telescope scans
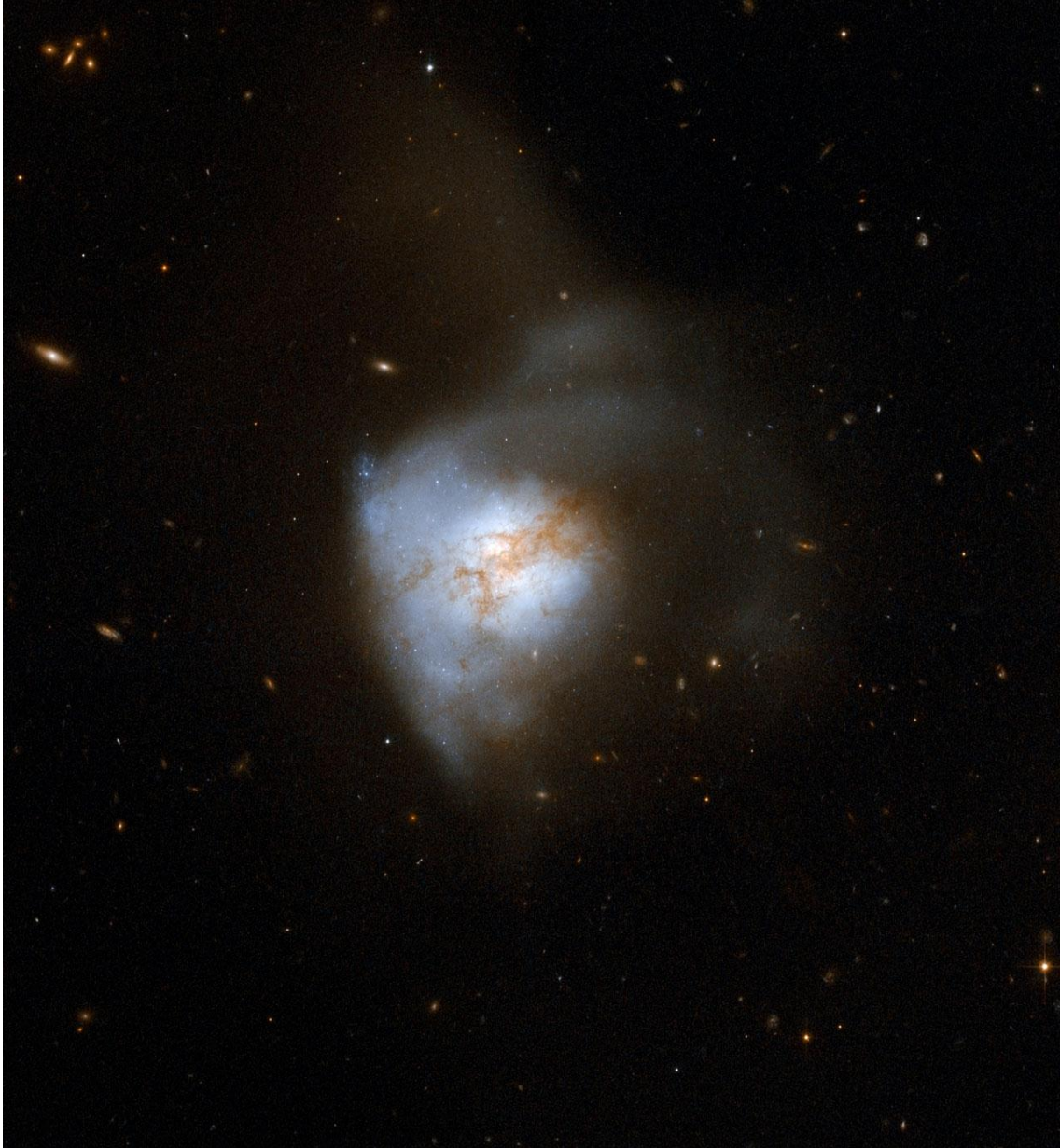
Figure 1.6: An optical image of Arp 220 from the Hubble Space Telescope (NASA et al. 2008). Because of the surrounding gas and dust, it is difficult to make out much of the interior structure of Arp 220, although the presence of extended tidal tails can be discerned.
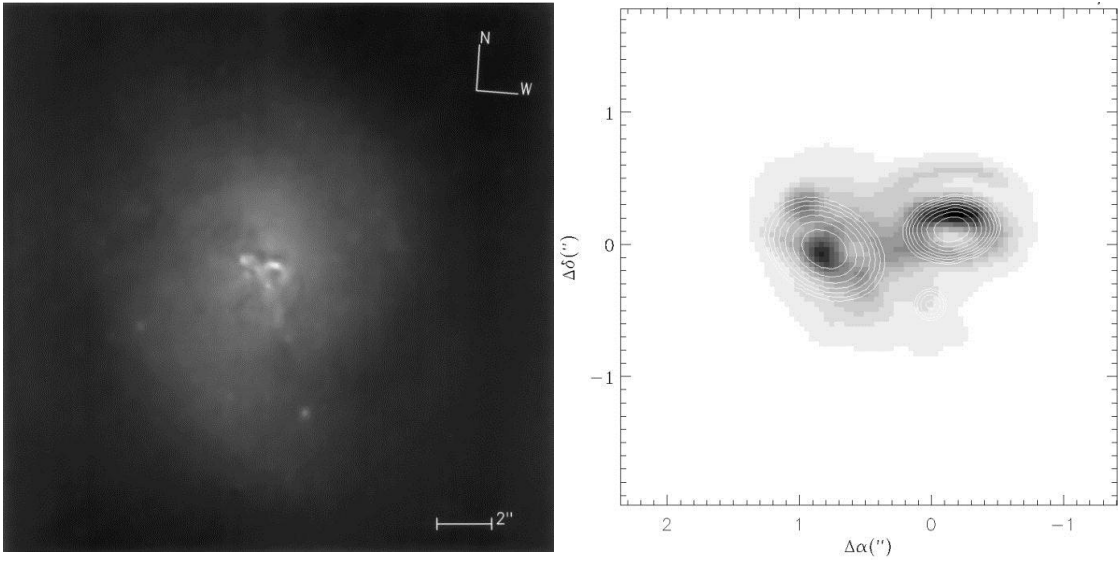
Figure 1.7: Left: Near-infrared (1.1, 1.6, and 2.22 μm) false color image of Arp 220 using the Near-Infrared Camera and Multiobject Spectrometer (NICMOS) camera on the Hubble Space Telescope (HST) with a 19″ field of view and 0.14″ resolution (in the lower right corner is an indication of the scale in arcseconds). Unlike the optical image (Figure 1.6), the twin nuclei of Arp 220 can be distinguished. Right: Contour image of 6 cm radio emission overlaid on the 2.22 μm image, showing that the nuclei observed in the IR image do coincide with the radio contour image. The coordinate axis are offset from the 2.22 μm peak located at $\alpha_{1950} = 15^{\mathrm{h}}32^{\mathrm{m}}46.90^{\mathrm{s}}$, $\delta_{1950} = +23°40'\ 07.94''$ (Scoville et al. 1998).
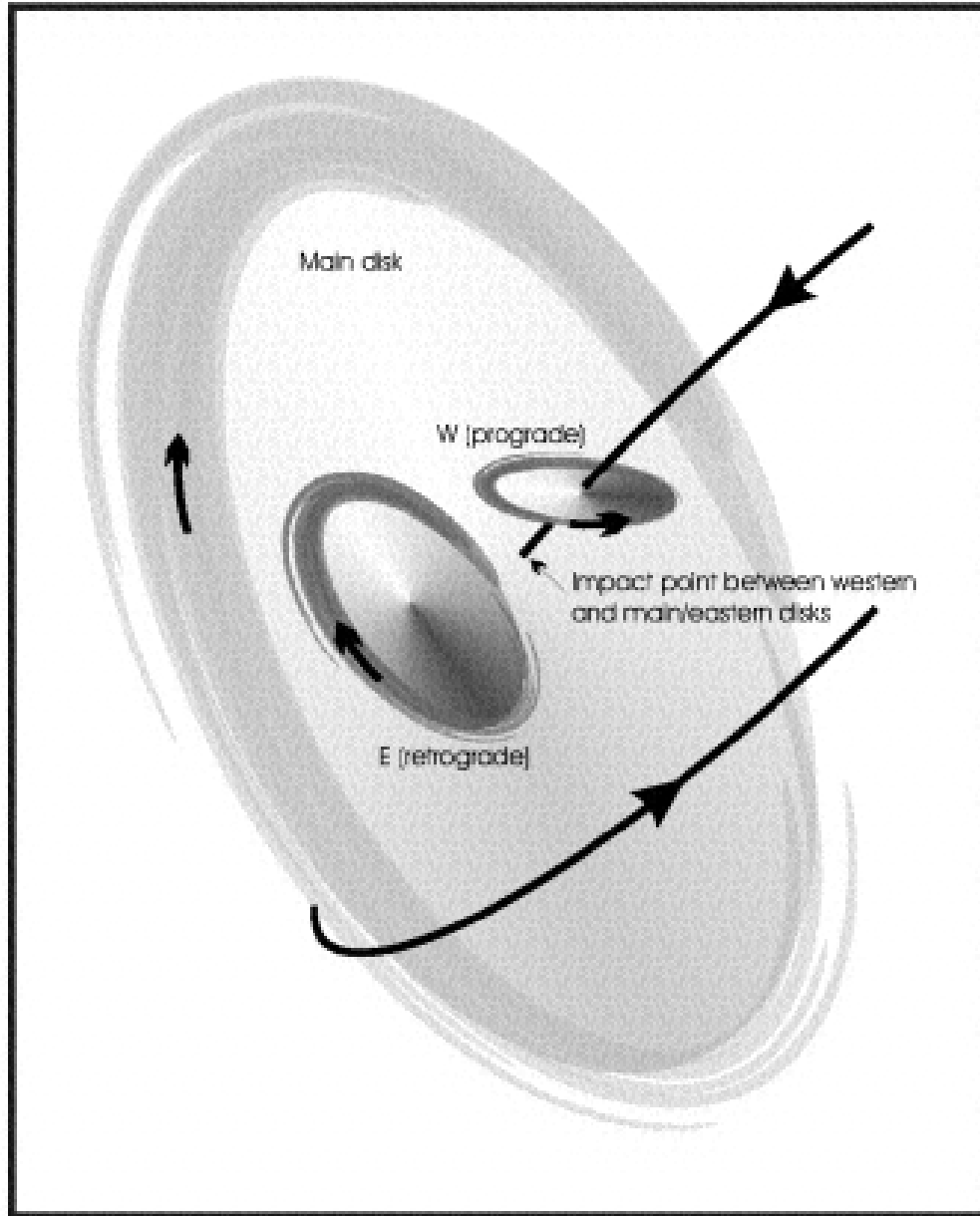
Figure 1.8: Diagram of the respective alignment and movement of the nuclei along with the kpc-scale CO disk of Arp 220, as prepared by Mundell et al. (2001). The small arrows indicate the rotation of the respective disks, while the large arrow indicates the path of the western nucleus with respect to the eastern nucleus.

a source across a range of frequencies in the hope of detecting new or previously undetected spectral lines toward that source. The Arecibo spectral survey toward Arp 220 was conducted between 1.1 GHz and 10 GHz. During this survey, numerous spectral line transitions were detected, some of them for the first time in Arp 220, and some of them for the first time in an external galaxy (Salter et al. 2008). The transitions observed in this survey are listed in Table 1.1. Being a single dish telescope, Arecibo has very poor angular resolution, (0.5′ - 3.5′ for the frequency limits of the survey). Therefore, in order to determine where the spectral lines originate in the structure of Arp 220, one must observe at higher angular resolution, such as with an interferometer like the EVLA (Figure 1.4). This thesis focuses on observing the direct l-type (J $= 5$) transition in the vibrationally excited $\nu_2 = 1$ state of HCN (Section 1.4) and the $1_{10} - 1_{11}$ transition of H_2CNH with the EVLA. Both these transitions were detected by Arecibo for the first time in an external galaxy. We should note though, that even though the spatial resolution of the EVLA will be improved by a factor of ~ 100 compared to Arecibo for these transitions, the velocity coverage of the EVLA with the old correlator (Section 2.1) is much smaller. This is clearly visible in Figure 1.9, which shows that the spectral lines observed by Arecibo have a much greater velocity/frequency coverage than our observations. Despite this, there were three main reasons why we chose to observe these lines with the EVLA. First, the $\nu_2 = 1, J = 5$ HCN line was the strongest line detected in absorption while the $1_{10} - 1_{11}$ transition of H_2CNH was the strongest line detected in emission in the 2008 Arecibo spectral survey; therefore, they are naturally the best lines to follow up with an interferometer with a higher spatial resolution. Second, these transitions are at frequencies (6612, 5196 MHz respectively) that are close enough together that they could be observed simultaneously with the existing capabilities of the EVLA in 2008 (Section 2.1), thereby acting as a demonstration of the then newly acquired EVLA bandwith. Finally, both these molecules are prebiotic molecules, as they can both be used to create the simplest amino acid, glycine (Section 1.4). Therefore, they have the potential of leading to future observations that would engage a much broader theme and community.

Table 1.1: List of Transitions Observed in the 2008 Arecibo Spectral Survey

Molecule	Transition	Rest Frequency (MHz)
Hydrogen Cyanide (HCN)	$\nu_2 = 1, \Delta J = 0, J = 2$	1346.7650^c
	$J = 4$	4488.4718^c
	$J = 5$	6731.9098^{ac}
	$J = 6$	9423.3338
Hydroxyl Radical (OH)	$2\Pi_{1/2}, J = 1/2, F = 0-1$	4660.242
	$F = 1-1$	4750.656
	$F = 1-0$	4765.562
	$2\Pi_{3/2}, J = 5/2, F = 2-3$	6016.746
	$F = 2-2$	6030.747
	$F = 3-3$	6035.092
	$F = 3-2$	6049.084
	$2\Pi_{1/2}, J = 3/2, F = 1-1$	7761.747^e
	$F = 2-2$	7820.125^e
	$2\Pi_{3/2}, J = 5/2, F = 2-2$	8135.870^e
^{18}OH^b	$2\Pi_{3/2}, J = 3/2, F = 2-2$	1639.503
Formic Acid (HCOOH)^b	1(1,0)–1(1,1)	1638.805
Methanol (CH$_3$OH)	$5_1 - 6_0 A^+$	6668.5192^d
Methanimine (H$_2$CNH)	$1_{10} - 1_{11}, \Delta F = 0, \pm 1$	5289.813^{ad}

[a] These were the transitions observed in this work.

[b] There was some ambiguity as to the identity of this detection, whether it was ^{18}OH or HCOOH that was detected, as both transitions have very similar rest frequencies.

[c] These were the first ever celestial detections of these transitions.

[d] This was the first time these transitions were detected in another galaxy located more than 10 Mpc away.

[e] This was the first time these transitions were detected in Arp 220.
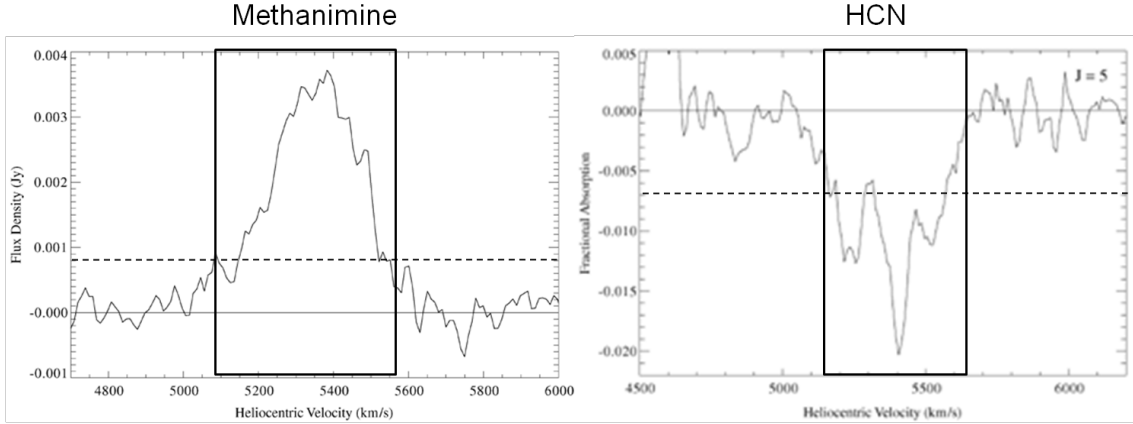
Figure 1.9: The corresponding H_2CNH and HCN spectral lines from the 2008 Arecibo Spectral Survey (Salter et al. 2008). The rectangular box in both panels shows the total velocity coverage of the EVLA observations reported in this thesis. While the velocity coverage is significantly narrower than Arecibo's, the EVLA observations have much better angular resolution. The dashed lines represent the EVLA sensitivity level of 2 sigma.

1.4 The Prebiotic Molecules H_2CNH and HCN

We chose to observe HCN and H_2CNH in this thesis for the three reasons discussed in Section 1.3.2 above. However these molecules also impact a wider subject area outside of the scope of this thesis in that they are both considered prebiotic molecules. These molecules can be used to create the simplest of the amino acids, glycine. Amino acids form the basis of all known life. There are 20 different amino acid monomers that form the protein enzymes that make the four organic bases (adenine, guanine, cytosine, and thymine). These bases form the different genetic codes in deoxyribonucleic acid, or DNA (Dickerson 1978). While observations for the existence of amino acids are beyond the scope of this thesis, we will nevertheless describe below three pathways for their formation from HCN and H_2CNH, if only to demonstrate that the connection is closer than one might imagine. For example, one pathway for the formation of glycine is when HCN and H_2CNH combine to form aminoacetonitrile which will then form glycine through hydrolysis, where hydrolysis is the process where water is split into a hydrogen cation (H^+) and a hydroxide anion

(OH^-), which can then combine with other molecules to produce other reactions. That is, we can have:

$$H_2CNH + HCN \rightarrow \underbrace{NH_2CH_2CN}_{\text{aminoacetonitrile}} \overset{hydrolysis}{\longrightarrow} \underbrace{NH_2CH_2COOH}_{\text{glycine}}, \qquad (1.4)$$
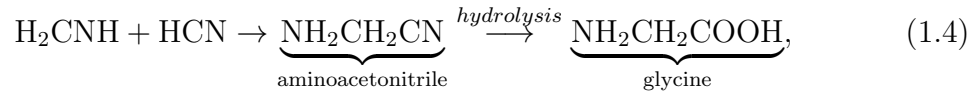
The process described in equation (1.4) above requires the presence of water. In fact, a $3_{13} - 2_{20}$ H_2O megamaser with a transition frequency at $\nu_0 = 183.310$ GHz has previously been detected in Arp 220 (Cernicharo et al. 2006). In our own Milky Way Galaxy, it has been determined that 183 GHz H_2O emissions occur in high mass star-forming regions such as Orion (Cernicharo et al. 1999) and Sagittarius B2 (Cernicharo et al. 1999). The presence of starbursts and supernovae imply that Arp 220 is also a high star-forming region.

A second pathway is for HCN to combine with an aldehyde in the presence of ammonia. The aldehyde would lose water, and add ammonia from its surroundings to form an imine. The imine would then combine with HCN to form aminonitrile. All of these processes would be reversible; however the amino acid would then be formed from the aminonitrile by hydrolysis (and therefore utilizing the previously generated water), which is irreversible. This process is shown in Figure 1.10. It has been observed in experiments simulating the conditions of the primitive Earth, where ammonia would have been available (Dickerson 1978). It is certainly conceivable that such a process could occur in Arp 220, as both ammonia and formaldehyde have been detected in Arp 220 (Takano et al. 2005; Araya et al. 2004).

Finally, a third pathway is for H_2CNH to combine with formic acid to produce glycine (Godfrey et al. 1973):

$$H_2CNH + \underbrace{HCOOH}_{\text{formic acid}} \rightarrow \underbrace{NH_2CH_2COOH}_{\text{glycine}}, \qquad (1.5)$$
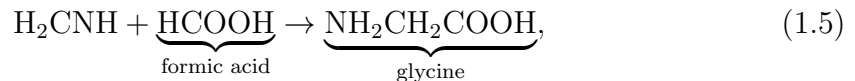
However, formic acid has yet to be definitively detected in Arp 220. The 2008 Arecibo Spectral Survey had an ambiguous detection that could be either ^{18}OH or formic acid (Salter et al. 2008). Formic acid has been previously detected in
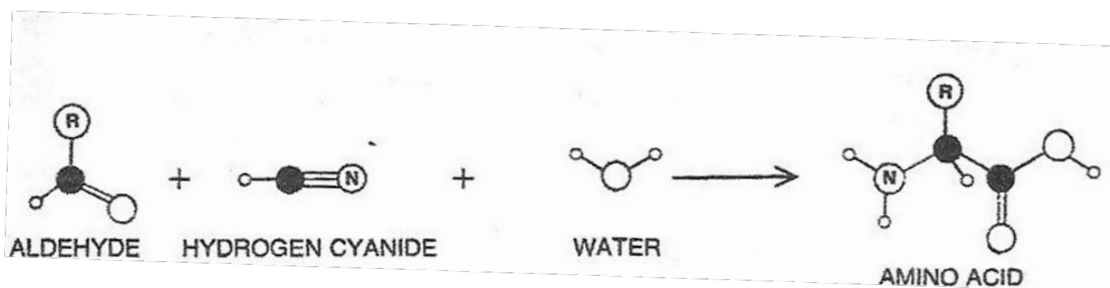
Figure 1.10: Diagram of the creation of an amino acid from the combination of an aldehyde and hydrogen cyanide. It is believed that this occurred in the atmosphere of the primitive Earth (Dickerson 1978).

interstellar clouds in our Galaxy (Godfrey et al. 1973), and it is therefore likely that it might also exist in Arp 220.

The observation of the H_2O megamaser and ammonia in Arp 220, combined with the results from the Arecibo spectral survey, shows the presence of all the reactants needed for glycine to be produced. What remains to be determined is if the reactants are actually located in the same area of Arp 220, and under the correct conditions for the reaction to occur. If such conditions can be confirmed, then the presence of glycine in Arp 220 could be inferred. However, this is beyond the scope of this thesis. Below, we discuss some structural aspects and other details of the molecules H_2CNH and HCN.

1.4.1 H_2CNH

The molecule H_2CNH is a member of the hydrogenation series that is based on the cyanide radical. The members of this series are: CN, HCN, H_2CNH, and H_3CNH_2. The first interstellar detection of H_2CNH was the $1_{10} \rightarrow 1_{11}$ transition in 1973 toward the star forming region Sgr B2 (Figure 1.11, Godfrey et al. 1973). A possible extragalactic detection of H_2CNH toward NGC 253 was reported by Martín et al. (2006), but remains uncertain due to low sensitivity and equipment problems. Therefore, the detection of H_2CNH in the 2008 Arecibo spectral survey (Salter et al. 2008) would be the first *definitive* extra-galactic detection of H_2CNH.
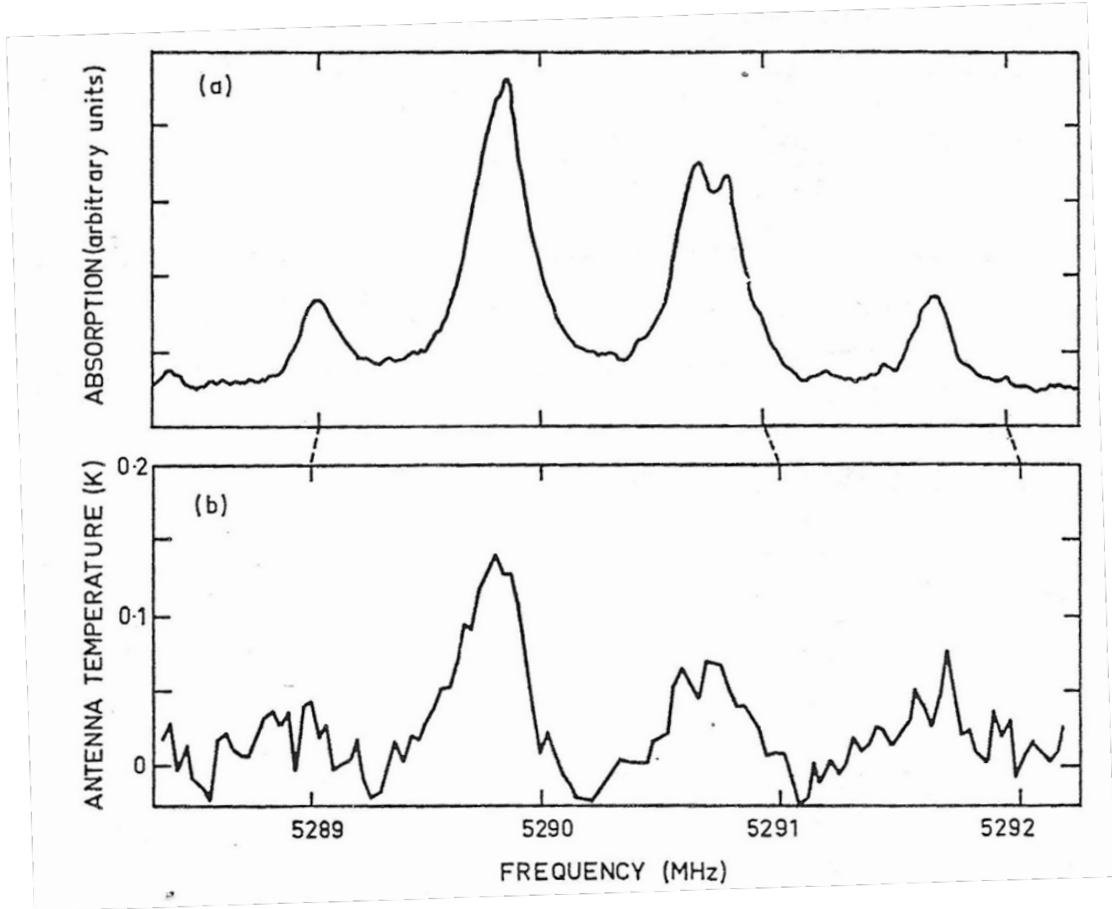
Figure 1.11: (a) The Laboratory spectrum of the $1_{11} \rightarrow 1_{10}$ transition of H_2CNH. The $1_{11} \rightarrow 1_{10}$ transition is the reverse of the $1_{10} \rightarrow 1_{11}$ transition (which was observed in this work), meaning that it occurs at the same frequencies, but that the $1_{11} \rightarrow 1_{10}$ transition occurs as an absorption (which is why the vertical axis is in terms of absorption), while the $1_{10} \rightarrow 1_{11}$ transition is an emission. It can be seen that there are six peaks spanning 3 MHz for this one transition. These peaks are the six hyperfine multiplets for this transition. (b) The observed emission of the $1_{10} \rightarrow 1_{11}$ transition of H_2CNH from Sgr B2 (Godfrey et al. 1973). The vertical axis is in units of Antenna Temperature (T_a), which is given by the relation: $P_a = g^2 k_b T^a \Delta\nu$ where P_a is power of the signal, g^2 is the voltage gain of the antenna, k_b is the Boltzmann constant, and $\Delta\nu$ is the bandwidth of the observation (Wrobel & Walker 2010).

Table 1.2: List of the Hyperfine Multiplets of Methanimine $1_{10} - 1_{11}$

Hyperfine Transition	ν_{rest} (MHz)[a]
$0 \leftarrow 1$	5288.968(4)
$1 \leftarrow 0$	5289.698(4)
$2 \leftarrow 2$	5289.816(4)
$2 \leftarrow 1$	5290.668(5)
$1 \leftarrow 2$	5290.827(5)
$1 \leftarrow 1$	5291.685(4)

[a] Godfrey et al. 1973

The $1_{10} \rightarrow 1_{11}$ transition of H_2CNH (which was the transition observed in this work) contains six hyperfine multiplets.The frequencies of the six multiplets are listed in Table 1.2, and span a range of about 3 MHz. The laboratory spectrum is shown in Figure 1.11, along with the observed line toward Sgr B2 from Godfrey et al. (1973). The six hyperfine components are clearly visible in both plots in this figure. The situation is different, however, for an external galaxy like Arp 220, where large scale motions will broaden each hyperfine to the extent that they blend in velocity and cannot be distinguished from one another. This is evident in Figure 1.12, where the frequencies corresponding to each of the six hyperfines are marked. The situation is made worse in Arp 220 due to the abnormally large velocity width observed for almost all molecular spectra (Takano et al. 2005). Such large velocity widths in Arp 220 have been ascribed to either rapidly rotating gas in the nuclear region due to an obscured active galactic nucleus (AGN)[2], or high velocity inflow or outflow of gas in the nuclear region, or violent turbulence caused by the galaxy-galaxy collision.

---

[2]An AGN is a compact region at the center of a galaxy that is known for having a high luminosity that can not be attributed to just stars (Peterson 1997).
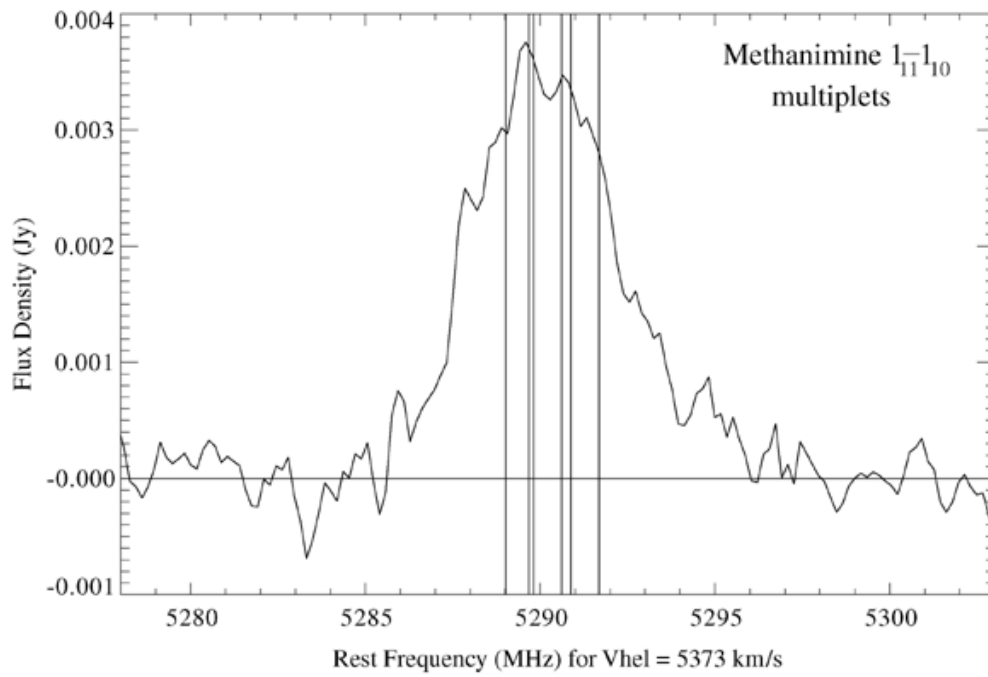
Figure 1.12: Spectrum of H_2CNH toward Arp 220 observed during the Arecibo survey, with the $1_{10} - 1_{11}$ hyperfine multiplets indicated by vertical lines (Salter et al. 2008). The reason for the broad linewidth that prevents identification of individual hyperfine components is discussed in Section 1.4.1.

1.4.2 HCN

The molecule HCN is well known in astronomy as a tracer of dense molecular gas, $n(H_2) > 10^4$ cm^{-3} (e.g., Rolffs et al. 2011; Cernicharo et al. 2011; Christopher et al. 2005; Wu et al. 2005; Morris et al. 1974), and is the prototypical tracer of dense gas content in ULIRGs and other distant luminous galaxies (Solomon et al. 1992; Curran et al. 2000; Sakamoto et al. 2011). HCN is a linear molecule composed of three atoms, which results in four vibrational modes. In general, a linear molecule with N atoms has $(3N - 5)$ vibrational modes (Thorwirth et al. 2003). Two of these are due to the stretching of the C—N (ν_1) and C—H (ν_3) bonds. The other two modes arise from the bending of the H—C—N molecule (ν_2). These two bending modes are degenerate as the molecule can bend in two different orthogonal planes. For example, if the HCN molecule is aligned along the y axis, then it would be able to bend in both the $x - z$ and the $x - y$ planes (Figure 1.13). This degeneracy is lifted when the molecule is both bending and rotating at the same time, which results in a phenomenon called l-type doubling. Another way of looking at this is to think of the degenerate bending mode as having components of an additional angular momentum $p = l\hbar$ about the linear axis of the molecule, where the quantum number l can take values v, $v - 2$, $v - 4$, ..., $-v$; by convention ν is used to refer to a certain vibrational mode (as stated above: ν_1 and ν_3 are stretching modes; ν_2 is the bending mode), whereas v is used for the vibrational quantum number.

We will now look at the first excited vibrational bending mode ($\nu_2 = 1$) of HCN in more detail, since the HCN spectral line observed in this thesis belongs to this state. Since the vibrational quantum number for this state is $v = 1$, we get two values for l: v, and $v - 2 = -1 = -v$; that is, $l = +1, -1$. This means that every rotational level in the $\nu_2 = 1$ state is split into two sublevels. Therefore, two different types of transitions are now possible: the ones with $\Delta J = \pm 1$, and the ones with $\Delta J = 0$. The latter type of transitions with $\Delta J = 0$ are called "direct l-type transitions" (Figure 1.14). For example, the HCN spectral line observed in this thesis is the direct l-type transition in the first excited vibrational state ($\nu_2 = 1$)
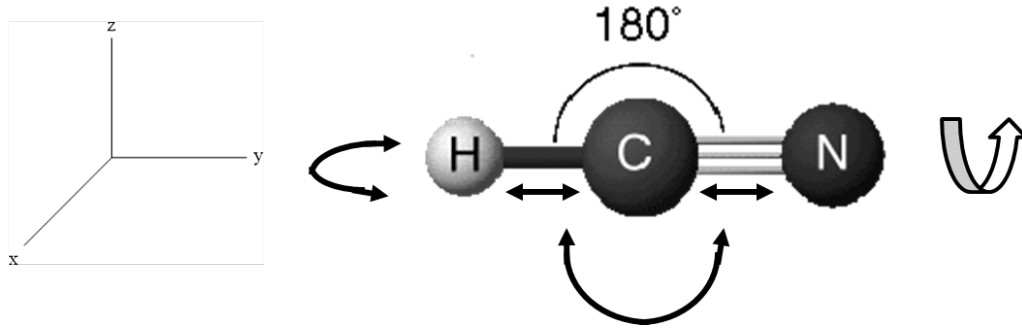
Figure 1.13: Diagram of the different stretching and bending modes of the linear molecule HCN (black arrows). Note that the two bending modes (curved black arrows) are degenerate unless some rotation (white arrow) is occurring, as the angular momentum imparted by the rotation lifts the degeneracy.

that occurs due to the splitting of the $J = 5$ rotational level.

Direct l-type transitions in HCN were first measured in the laboratory by Shulman & Townes (1950). As the splitting is rather small for a given J, these transitions occur at low frequencies, and many are observable with radio telescopes. For the first excited vibrational bending mode ($\nu_2 = 1$), the frequencies are given to first order by $\nu = qJ(J + 1)$, where the l-type doubling constant $q \approx 224$ MHz for the $\nu_2 = 1$ state of HCN. Therefore, many of these transitions are accessible to cm-wave radio telescopes. Examples of existing observations of direct l-type transitions in the $\nu_2 = 1$ state of HCN are the $J = 8$ through $J = 14$ transitions toward the proto-planetary nebula CRL 618 with the single dish Effelsberg telescope (Thorwirth et al. 2003), the $J = 9$ through $J = 13$ transitions toward very early stages of high mass star forming regions called hot molecular cores with the Effelsberg telescope (Rolffs et al. 2011), and the $J = 2, 4, 5, 6$ transitions toward Arp 220 with the Arecibo telescope (Salter et al. 2008). Astronomically, transitions in the $\nu_2 = 1$ vibrationally excited state are of interest because this state lies about 1000 K above the ground vibrational state, and therefore it traces highly excited dense molecular gas. Direct l-type transitions up to $J = 14$ in the $\nu_2 = 1$ state should be accessible with an interferometer once the full capabilities of the EVLA are in place.
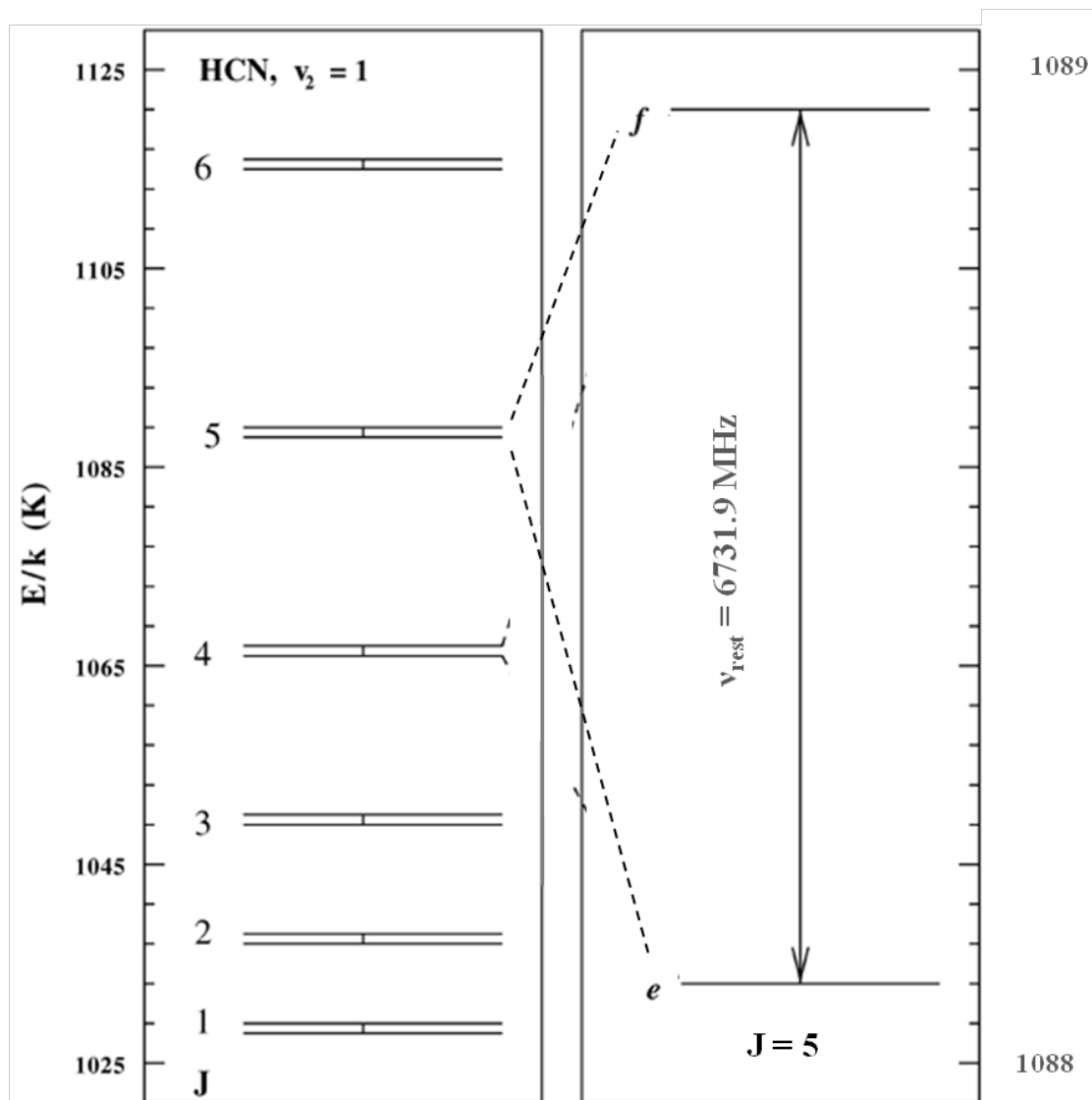
Figure 1.14: Energy diagram for HCN in the $\nu_2 = 1$ state, with the corresponding $\Delta J = 0$ shown from $J = 1$ to $J = 6$ (Salter et al. 2008). The panel on the right shows the $J = 5$ direct l-type transition in more detail, which was the transition observed in this work.

1.4.3 Masers

As it is likely that the H_2CNH spectral line toward Arp 220 is from a maser, we will now discuss some details of masers. Maser is short for microwave amplification by stimulated emission of radiation, just like how laser stands for light amplification by stimulated emission of radiation. Masers are the same as lasers, except that lasers occur in the visible spectrum, and masers occur at the microwave/radio spectrum. Both operate through stimulated emission for states that have undergone a population inversion. Population inversion is when there are more molecules or atoms in excited states than in the ground state (Saleh & Teich 1991). This is usually achieved by some sort of energy pump. In astrophysical masers, the masing medium is usually molecular gas (e.g., H_2O, OH, CH_3OH), and the energy pump is either collisional (e.g., H_2O masers, Liljeström & Gwinn 2000) or radiative (e.g., 6.7 GHz Class II CH_3OH masers, Goldreich & Kwan 1974). When electromagnetic waves are incident on gas that has undergone a population inversion, stimulated emission occurs as the molecules drop to a lower energy level. As the emitted radiation passes through long columns of gas and dust, it is amplified along directions that have the required velocity coherence. For example, a maser could be formed in the galaxy Arp 220 by the amplification of the continuum emission of the nucleus by the molecular gas associated with the starburst regions found at the nuclei (Baan & Haschick 1995). Masers are of interest in astrophysics because they provide compact intense sources that can therefore be easily measured by interferometers at high angular resolution. Due to the much larger brightness of masers, it is possible to use them to measure the rotation rate and size of galaxies and their nuclei (Narvey-Smith 2011). Megamasers are particularly bright masers that tend to occur in active galaxies that contain a large amount of molecular gas.

In the next chapter we will discuss our observations of the 5289.8 MHz $1_{10} \rightarrow 1_{11}$ H_2CNH emission line and the 6731.9 MHz J=5 direct l-type vibrationally excited ($\nu_2 = 1$) HCN absorption line.

CHAPTER 2

Observations and Data Reduction

This thesis presents observations of HCN and H_2CNH spectral lines toward the merging galaxy Arp 220. The observations are discussed in Section 2.1, the data reduction is described in Section 2.2, and the methods of visualization and additional processing are described in Section 2.3.

2.1 Observations

The observations for this work were conducted in December of 2008 with the EVLA (Project Code AM 969, PI: E. Momjian). The EVLA is an upgraded version of the old Very Large Array (VLA) radio interferometer. The upgrade started in 2008 and is scheduled to finish in 2013. The upgrade consists of replacing some of the receivers on the 27 existing antennas and adding additional receivers. This would then make the EVLA capable of observing the entire range of frequencies between 1 to 50 GHz with a sensitivity greater than the old VLA by a factor of 5-20. The upgrade will also replace the old VLA correlator with a Wide-band Interferometric Digital Architecture (WIDAR) correlator that will allow handling of up to 8 GHz bandwidth (compared to the the 50 MHz bandwidth with the old VLA correlator) with a spectral resolution of up to 0.2 Hz (compared to the 381 Hz resolution using the old VLA correlator, Ulvestad et al. 2006). The projected replacement and addition of receivers is shown in Figure 2.1. Due to this upgrade, our observations had access to only limited capabilities of the EVLA. During these observations (December 2008), only 16 of the 27 antennas in the array were retrofitted to EVLA standards that provide flexible tuning capabilities and frequency coverage suitable for these observations (Figure 2.2). The 6 cm C-band receivers were chosen for the observations reported in this thesis because the observed frequencies of 5196

MHz for H_2CNH (ν_{rest} = 5289.8 MHz) and 6612 MHz for HCN (ν_{rest} = 6731.9 MHz) lie within the frequency range of 4000 to 8000 MHz of these receivers. The observations were conducted using two spectral windows, one centered at 5196 MHz for H_2CNH, and the other at 6612 MHz for HCN. Each of these spectral windows had a 12.5 MHz bandwidth and 15 channels, yielding a spectral resolution of 781.25 kHz, corresponding to a velocity resolution of 45 km/s for H_2CNH and 35 km/s for HCN (the difference in velocity resolution is due to the difference between the rest frequencies of H_2CNH and HCN, see Section 1.1). The bandwidth and spectral resolution are very limited because the new WIDAR correlator of the EVLA was not functional in December 2008; instead, the old VLA correlator had to be used. During our observations in December 2008, the EVLA was in the A-configuration. In the A-configuration, the individual antennas are separated by the largest amount. Such long baselines (up to 36 km) allow for the highest resolution possible with the EVLA (0.4″ at C band). The total observing time was 10.5 hours, with 8 hours on Arp 220 and the rest of the time spent on antenna movement and on the calibrators: 1331+305 (flux calibrator, also known as 3C286), 1513+236 (phase calibrator), and 1602+334 (bandpass calibrator). Each type of calibrator is used in interferometric radio observations for a specific purpose, which will be discussed in greater detail in Sections 2.2.2 and 2.2.3.

2.2 Data Reduction

All data reduction was performed using the Astronomical Image Processing System (AIPS) software package provided by the National Radio Astronomy Observatory (NRAO). The AIPS software contains a variety of "tasks" which are in essence different programs within the software package designed to perform very specific actions. The data reduction steps are discussed in more detail below. A summary of the AIPS tasks used is provided in Table 2.1. In all the sections below, tasks in AIPS are denoted by italicized uppercase letters.
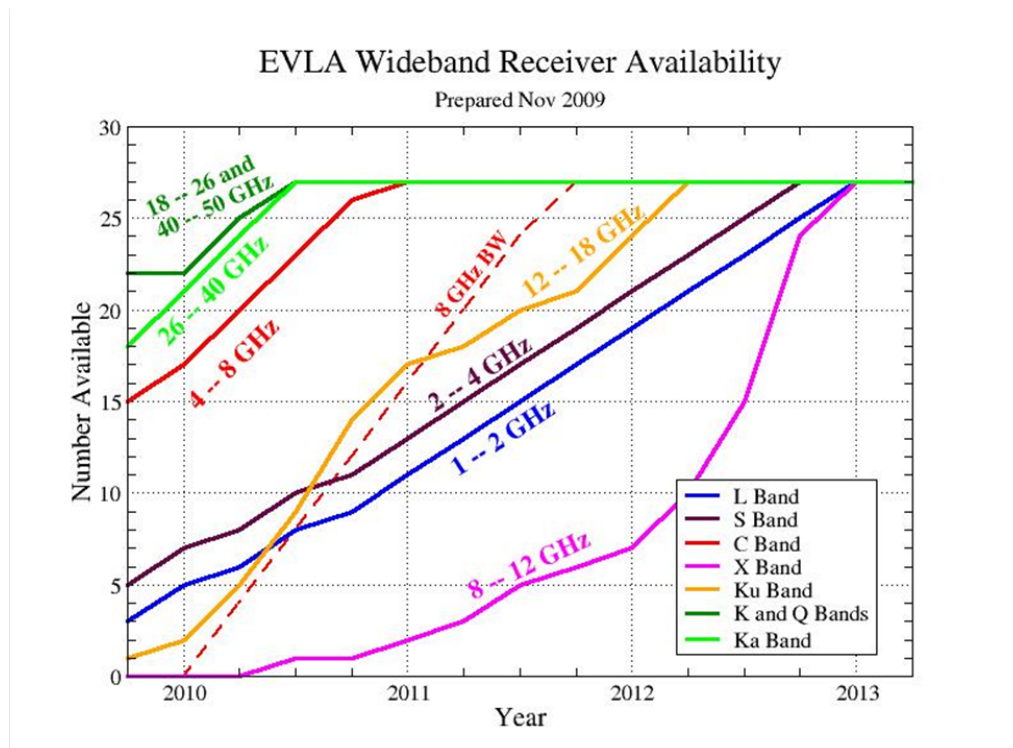
Figure 2.1: Projected timeline for the replacing of the old VLA receivers with new EVLA receivers, as of November 2009 (NRAO 2009). It can be seen that not all the EVLA style C-band receivers (which is the band that the observations for this work were performed at) were installed at the end of 2008, which was when the observations for this work were made.
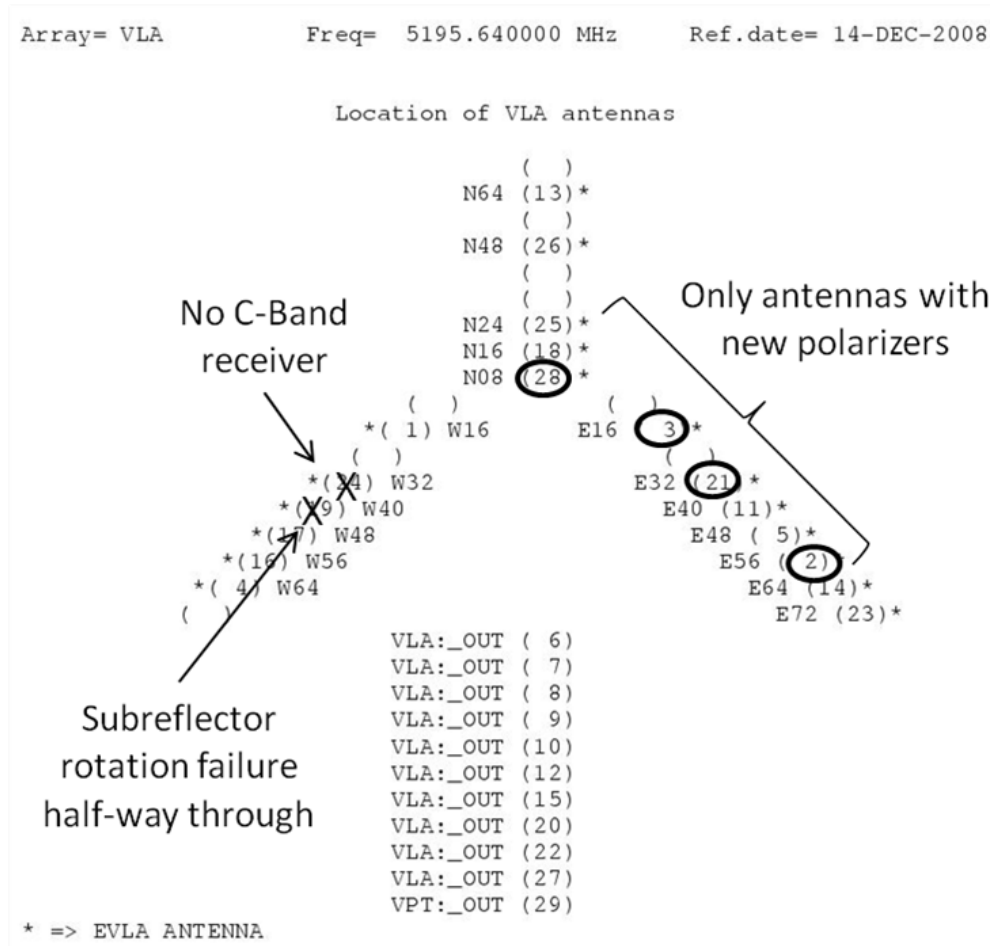
Figure 2.2: Diagram of the location of the EVLA antennas on the day of the observation. At the bottom is a list of all the antennas that were not available due to the VLA to EVLA transition. Only 16 of 27 antennas were available for our observations.

Table 2.1: Summary of AIPS Tasks Used

EDITA *TVFLG* *UVFLG*	Used to view and flag the data in different ways.
SETJY	Used to set the flux density of the flux calibrator.
CALIB	Primary calibration task used to calibrate data with or without the use of a model.
GETJY	Used to generate the flux densities of the phase and bandpass calibrators.
CLCAL	Used to combine SN tables and apply to or create CL tables.
BPASS	Used to generate bandpass calibration.
IMAGR	Primary imaging task used to Fourier transform and deconvolve the data.
CNTR	Used to generate a contour plot.
KNTR	Used to generate a channel map overlaid on a contour plot.
ISPEC	Used to generate spectral line graphs.
TVSTAT	Used to obtain information from an image, such as RMS or peak flux values, by selecting the region of interest in the TV display.
IMSTAT	Similar to *TVSTAT*, used to obtain information from an image, such as RMS or peak flux values, by selecting the region of interest via user input on the command line.
MATH	Used to perform mathematics on an image, such as by multiplying or adding a constant value to the image.
PUTH	Used to modify the header of a file, e.g., to manually assign a desired unit to a quantity such as the flux density.
SPLIT	Used to create a file which contains only a portion of the entire data, such as data from only one source or from just specific frequency channels.
COMB	Used to combine two images using specific mathematical methods.
TRANS	Used to transpose the data matrices.
XSUM	Used to sum or average over an axis.
JMFIT	Used to fit a Gaussian to a portion of an image, e.g., to determine the size of an observed source.
FITTP	Used to output the AIPS files as FITS files, which can then be used by other programs (such as for the creation and adjustment of graphs and figures).

Flag Data

AIPS task used: *EDITA, TVFLG, UVFLG*

Flux & Phase Calibration

AIPS task used: *SETJY, CALIB, GETJY, CLCAL*

Bandpass Calibration

AIPS task used: *BPASS*

Create a Single Source Dataset

AIPS task used: *SPLIT*

Imaging & Deconvolution

AIPS task used: *IMAGR*

Self Calibration

AIPS task used: *CALIB, IMAGR*

Satisfactory Image?

No

Yes

Visualization & Additional Processing

AIPS task used: *KNTR, ISPEC, MATH, COMB, XSUM*

CARMA software: *WIP*

Figure 2.3: Flowchart depicting a summary of the steps involved in this work and the AIPS task used in each step (see Table 2.1 for a summary of the AIPS tasks).

2.2.1 Flagging

The first step in the data reduction process is usually the flagging of bad data. Such bad data may be present due to isolated and transient antenna or other equipment malfunctions that are not identified and flagged by the online system. The tasks *EDITA*, *TVFLG*, and *UVFLG* were run to view the data in different ways and mark any bad data in a flag (FG) table. Flagged data are not actually deleted, but instead identified in a flag (FG) table appended to the data set. The data that have been included in this FG table can then be removed from consideration by any later tasks that are run on the data set.

2.2.2 Flux and Phase Calibrations

The second and third steps in the data reduction process are the flux and phase calibration. These steps are necessary because the visibilities (Equation 1.3) produced by the correlator are not the true visibilities that we desire. Rather, the true visibilities must be extracted from the observed visibilities by correcting for effects introduced by local atmospheric conditions and by the signal path in the instrument. This correction process is known as calibration. The standard procedure is to assume that the true visibility $V_{ij}(t)$ for correlation between the antennas i and j is related to the observed visibility $[V_{ij}(t)]_{\mathrm{obs}}$ by the equation:

$$[V_{ij}(t)]_{\mathrm{obs}} = g_i(t)\, g_j^*(t)\, V_{ij}(t) + \epsilon_{ij}(t), \qquad (2.1)$$

where $\epsilon_{ij}(t)$ is the thermal noise, and $g_i(t)$ and $g_j(t)$ are the gains of the ith and j^{th} antennas; the gain of an antenna is a complex number that represents the effects of atmospheric conditions and the signal path in the instrument. To facilitate calibration, one needs to observe flux and phase calibrators during the observation (and also bandpass calibrators for spectral line observations, whose objective will be described below). The calibrators are usually point sources or sources with known structure so that they have predictable visibilities. The process of calibration can then be viewed as an attempt to measure the complex numbers $g(t)$ that specify

the gains of the antenna by comparing the observed visibilities of calibrators to their predicted visibilities. Just like the flagging process, calibration does not affect the actual data set. Instead solution (SN) and calibration (CL) tables are created and appended to the data set. These contain the results of running the calibration tasks, and can then be incorporated into all the later tasks that are carried out on the data.

The VLA periodically monitors the intensities of about 5 point sources that have been designated as flux calibrators because they have very stable behavior over time. As mentioned in the previous section, we chose to observe the flux calibrator 1331+305. We ran the AIPS task *SETJY* to determine the flux of this source, and to save it into a source (SU) table attached to the data. The task *CALIB* was then run three times, first on our flux calibrator (1331+305), then on our phase calibrator (1513+236), and finally on our bandpass calibrator (1602+334). Each run of *CALIB* compares the observed visibility phases of the specified calibrator with the predicted visibility phases for a point source or a specified model if the calibrator has structure. Each of these runs created a separate solution (SN) table that was appended to the data set. At this stage, the SN table for the flux calibrator (1331+305) contains the correct antenna gain amplitudes, because its flux density has already been inserted into the SU table with *SETJY*. However, the SN tables for the phase and bandpass calibrators still do not have the correct antenna gain amplitudes. The task *GETJY* was then run to determine the flux densities of the phase and bandpass calibrators. This task compares the SN tables for the phase and bandpass calibrators with the SN tables of the flux calibrator, and uses the amplitude level of the flux calibrator to enter the correct result for the flux density of the phase and bandpass calibrators into the source (SU) table, and then correct the antenna gain amplitudes of the solutions in the SN tables for the phase and bandpass calibrators. At this stage, we have solved for and obtained the complex numbers $g(t)$, which are the gains for all the antennas for the time ranges of all the calibration scans. The final step in the calibration process is to interpolate the solutions in the SN tables derived from the calibrators into a calibration (CL) table
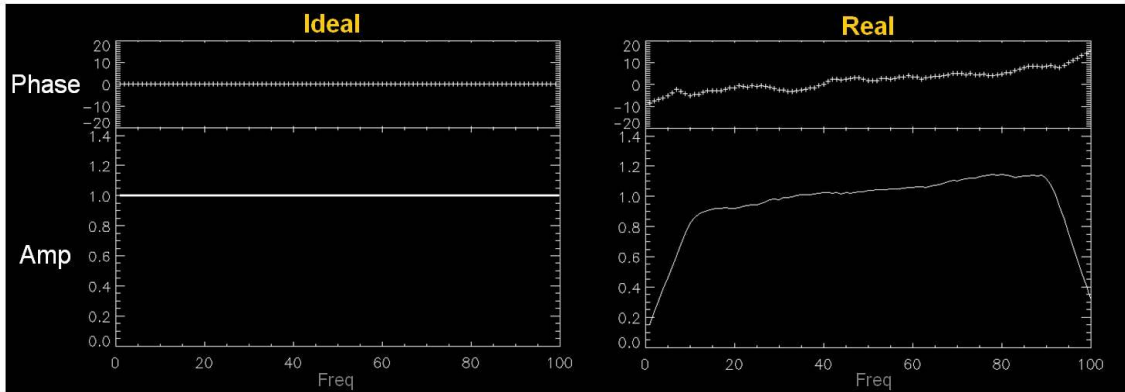
Figure 2.4: (Left) Display of the observed amplitude and phase of different frequencies for an ideal bandpass situation, where the phase is zero and the amplitude is constant for all frequencies. (Right) Display of a more realistic amplitude and phase for different frequencies. Due to the imperfect attenuation of the bandpass filter in the antenna, the edge frequencies contain steeply sloping artifacts, while the amplitude plateau may also contain a slope. Despite phase calibration already being applied, which adjusts the phase based on observations of a phase calibrator source (for this work 1513+236 was used), the frequencies can still contain non-zero phases. To help eliminate these artifacts, a bandpass calibration must be performed (Pihlström 2010).

for all the sources, including the target source, Arp 220. This was done using the AIPS task *CLCAL*.

2.2.3 Bandpass Calibration

The fourth step in the data reduction is the bandpass calibration. This is necessary for spectral line observations because both the amplitude and phase of the complex numbers $g(t)$ that specify the gains of the antennas (Equation 2.1) may vary across spectral channels as the filters used to set the bandpass do not have idealized linear responses across the entire band (Figure 2.4). The observed bandpass calibrator (1602+334) fulfilled the criterion of a reasonably strong point source that has a flat response across the frequency band. We used the AIPS task *BPASS* to carry out the bandpass calibration. The result is a bandpass (BP) table that is appended to the data.

2.2.4 Applying the Calibration

After the steps outlined above have been completed, the observed visibility data (Equation 1.3) remain unaffected. As described above, the results of all the steps have been written into FG, CL, and BP tables that have been appended to the dataset. The results of prior steps have been applied during the running of tasks following these steps, but none of them have operated directly to change the data. At this stage, we ran the AIPS task *SPLIT* to apply the FG, CL, and BP tables to the data and write out a new single source dataset. This dataset contains the calibrated visibility data for our target source, Arp 220. Henceforth, we will deal only with this calibrated Arp 220 dataset.

2.2.5 Imaging

The calibrated Arp 220 dataset mentioned in the previous section contains the visibility data for Arp 220 with the results of all our calibration steps applied to it. The next step is to Fourier transform these data so that we have an intensity map of the source at a particular frequency. In other words, we must obtain a map of the sky with Right Ascension (R.A.) along one axis and Declination (Dec) along a perpendicular independent axis that contains the target source (Arp 220). Moreover, we have a spectral line dataset with 15 frequency channels for the HCN observations, and 14 frequency channels for the H_2CNH observations (one of the channels had to be removed during the flagging process). This means that we must obtain 15 such images, each separated by 781.25 kHz or, equivalently, 35 km/s for the HCN observations, and 45 km/s for the H_2CNH observations in velocity. Together, this will give us a spectral cube for the operations described in Section 2.3. However, a mere Fourier transform from the visibility plane to the image plane will not achieve the intended purpose. This can be understood if we think of the visibility plane as a set of points with each point corresponding to a specific pair of EVLA antennas. Since we have 16 antennas in our observations, there are $16(16-1)/2$ points in the visibility plane at any given time. Next, if we imagined ourselves positioned at the

target source looking at the EVLA, we would notice that the distance between each pair of antennas changes as the Earth rotates. Therefore, each of these instances in time populates a different part of the visibility plane. However, due to the limited number of antennas, their positions with respect to each other, and the allowed time for the observations, we cannot populate every point in the visibility plane. This means that we must define a sampling function S that is equal to 1 for populated locations in the visibility plane, and zero at all other locations. A Fourier transform of the visibility plane therefore produces what is known to radio astronomers as a "dirty" image. It can be demonstrated mathematically that the dirty image is the desired "clean" image convolved with a so-called "dirty" beam which is the Fourier transform of the sampling function. To find the true intensity image, we must "deconvolve" the dirty beam from the dirty image.

We used the AIPS task *IMAGR* to carry out the Fourier transformation and deconvolution. We used the standard deconvolution procedure in *IMAGR*, which is based on the Clark-Hogbom algorithm (Högbom 1974; Clark 1980). This deconvolution algorithm works by repeatedly scanning the Fourier-transformed dirty image for the position with the highest intensity, each time subtracting from the dirty image the product of this maximum intensity times the dirty beam times a damping factor known as the loop gain that determines how quickly the deconvolution proceeds; we left the loop gain at the default value (0.1). This process continues until no peaks are found above some user-defined flux limit; we followed convention and set this limit to 3 times the root mean square (RMS) noise limit of 0.26 mJy/beam. The intensities of the points accumulated during these scans (called the "clean components") are then convolved with the "synthesized" beam to obtain the desired image, where the synthesized beam is an elliptical Gaussian that has been fit to the central lobe of the dirty beam. It is customary to express the angular resolution of the observations by stating the major and minor axes of this Gaussian measured at half the peak intensity, and calling it the synthesized beam (with half power bandwidth, or HPBW, appended in some cases). In our case, the synthesized beam for the HCN spectral line observations was $0.3333(6)'' \times 0.2801(0)''$, and for

the H_2CNH spectral line observation was $0.4020(1)'' \times 0.3409(8)''$.

2.2.6   Self Calibration

In cases where the target source has reasonably high flux, one can improve on the calibration by using the target source as its own calibrator. This is known as self calibration. In this process, one begins with an initial model of the source, usually taken from an initial image prepared as described in Section 2.2.5 above, or even from a point source model. In our case, we used the clean components from the first image. This model is supplied to the AIPS task *CALIB*, which then compares the observed visibilities with the visibilities corresponding to the supplied model, and uses Equation 2.1 to solve for the complex numbers $g(t)$ that specify the gains of the antennas. These complex gain solutions are then used with the input visibilities in Equation 2.1 to generate a set of corrected visibilities. The corrected visibilities are then Fourier transformed and deconvolved with *IMAGR*. The clean components obtained in the imaging process (Section 2.2.5) then become the model for the next iteration with *CALIB*. This process, pairing *CALIB* and *IMAGR*, is continued until a satisfactory set of antenna complex gain solutions is obtained; this is usually determined by the user by looking at RMS noise in the image and the source structure. In our case, we ran about five iterations of phase-only self calibration (in which we solved only for the phases of the antenna gains), followed by about a dozen iterations in which we solved for gain amplitudes and phases. The self calibrated visibility data are then almost ready for final imaging.

2.3   Visualization and Additional Processing

The self calibrated visibility data for H_2CNH and HCN were Fourier transformed and deconvolved using the procedure described in Section 2.2.5 after removing the continuum using the AIPS task *UVLIN*. Most astronomers prefer to implement this step of removing the continuum because the emission and absorption data are then displayed with a baseline at zero intensity (Figures 3.3 & 3.5). An image of the

continuum was also generated by splitting off one channel at the edge of the HCN dataset and Fourier transforming and deconvolving it (Section 3.1). After preparing the spectral line data cubes for H_2CNH and HCN, we looked at two different but complementary representations of the data. These are described in Section 2.3.1 below. Further processing of the data involved preparing images for measuring column densities; this is described in Section 2.3.2 below.

2.3.1   Visualization

We looked at two complementary representations of the spectral line data. First, we looked at maps of the H_2CNH emission and HCN absorption that showed the location of Arp 220 where the emission or absorption is taking place. We prepared these using the AIPS task *KNTR* to generate maps of the frequency channels with the highest emission (for H_2CNH) and absorption (for HCN), overlaid on contour plots of the 6.6 GHz continuum.

Second, we looked at spectral line plots, which are plots of the flux density versus the frequency. These were generated using either the AIPS task *ISPEC* (for initial examination) or using the WIP software from the CARMA array (for final plots included in this thesis). While the channel maps provide a very good visual representation of the locations in Arp 220 where the H_2CNH emission or HCN absorption is taking place, spectral line plots can be used to calculate quantities like the brightness temperature for emission lines (Section 3.2.2) and the optical depth for absorption lines (Section 3.3.2).

2.3.2   Column Density Image

The physical meaning of column density is discussed in Section 3.3.3. Here, we will only describe the procedure to prepare images from which column densities can be measured. First, the AIPS task *MATH* was used to multiply the data points in the HCN spectral line data set by -1. This produced a new spectral line image cube, in which the absorption line was effectively inverted so that it would look

like an emission line. This step was necessary because the code that calculates the optical depth will not work on negative data values. The task *COMB* was then used to operate on this modified HCN spectral line cube, together with the continuum image, to obtain the optical depth in each frequency channel for HCN; the optical depth is defined and explained in Section 3.3.2. Finally, the integration of optical depths that is required to calculate values for the column density (Section 3.3.3) was carried out using the AIPS tasks *TRANS* and *XSUM*. The task *TRANS* was required to transpose the axes in the optical depth cube (from xyz to zxy) because *XSUM* only adds values along the first axis. The significance of the column density is discussed in Section 3.3.3.

CHAPTER 3

Results and Discussion

In this chapter, the results of the observations described in Chapter 2 are presented and discussed. In Section 3.1, the continuum structure of Arp 220 is presented and compared to previous observations in the literature. The H_2CNH spectral line observed in emission toward the western nucleus of Arp 220 and the HCN spectral line, which was also observed toward the western nucleus of Arp 220 but in absorption, are presented and discussed in Section 3.2 and Section 3.3 respectively. Both of these are new results that have not been previously reported.

3.1 Arp 220 Continuum

Figure 3.1 shows a contour plot of the continuum from Arp 220 at 6612 MHz. The two nuclei are clearly visible in this image. The western nucleus has a peak flux of 80 mJy/beam and an integrated flux density of 108 mJy, while the eastern nucleus has a peak flux of 52 mJy/beam and an integrated flux density of 93 mJy, which are consistent with previous 6 cm VLA observations (Norris 1988). Also visible in our image are small protrusions to the northwest (top right) and southeast (bottom left). The protrusions are believed to correspond to the tidal tails that have been observed in optical wavelengths (Norris 1988; Wiedner et al. 2002). Finally, the larger kpc-scale CO disk is not detected in the 6612 MHz continuum, which is also consistent with previous observations (Norris 1988). Although the results described in this section are not new results, this discussion has been presented to verify that the observed continuum is consistent with previous observations. The following sections will then describe the new results of this work for the H_2CNH and HCN spectral lines.

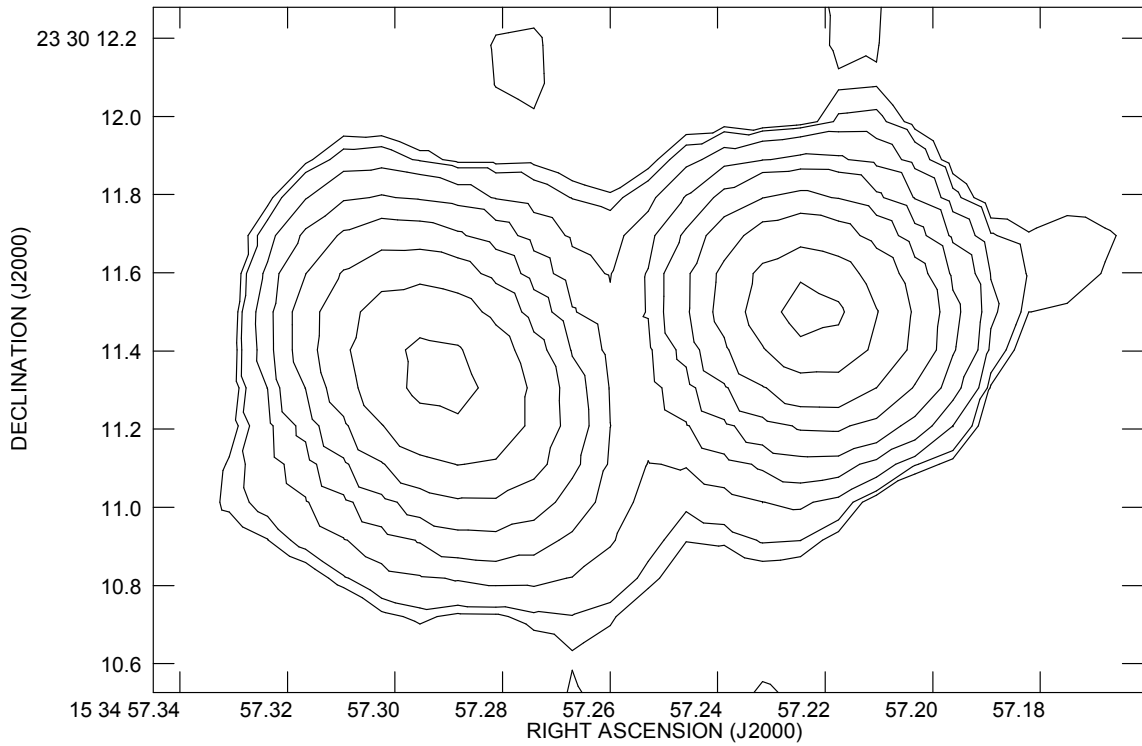Figure 3.1: Contour image of the 6612 MHz Arp 220 continuum from our observations. The RMS for the image is 0.23 mJy/beam. The contour levels are $(2, 3, 6, 12, 24, 48, 96, 192, 300) \times$ RMS. The $2 \times$ RMS contour has been added because it visually emphasizes the hint of protrusions to the northwest (top right) and southeast (bottom left) which have been seen in previous observations of Arp 220 (Norris 1988).

3.2 H$_2$CNH

The $1_{10} \rightarrow 1_{11}$ line of H$_2$CNH was observed in emission toward Arp 220. In Section 3.2.1, we present the results of these observations by looking at the channel map and the observed spectral line profile. We use the parameters of the observed emission line to measure the brightness temperature in Section 3.2.2, and use this measured value to demonstrate that the H$_2$CNH emission toward Arp 220 is likely maser emission. The isotropic luminosity of this maser is calculated, and compared to typical isotropic luminosities of H$_2$O masers in several different environments.

3.2.1 Spectral Line and Channel Map

Figure 3.2 shows a map of H$_2$CNH emission toward Arp 220. This was obtained by plotting the channel with the highest emission as described in Section 2.3.1. Figure 3.3 shows the H$_2$CNH spectra toward the two nuclei of Arp 220. From both figures it is clear that H$_2$CNH is detected in emission solely toward the western nucleus. In Figure 3.2 emission is seen only toward the western nucleus. In Figure 3.3 the H$_2$CNH spectrum toward the western nucleus has a line peak of 2.9 mJy/beam. As the RMS (noise) of the line is 0.3 mJy/beam, this means that we have a $\sim 10\ \sigma$ detection of the line. Meanwhile, there is no peak in the line toward the eastern nucleus that is above the RMS limit, signifying a non-detection toward the eastern nucleus. This localization of the H$_2$CNH emission to the western nucleus is a new result based solely on the observations reported in this work.

3.2.2 Brightness Temperature

In order to better understand the physical aspects of a radiating source, it is standard practice to calculate the brightness temperature. The brightness temperature (T_b) is defined as the Rayleigh-Jeans temperature of a black body that will give the same power radiated per unit area, frequency, and solid angle as the observed radio source, and is given by:
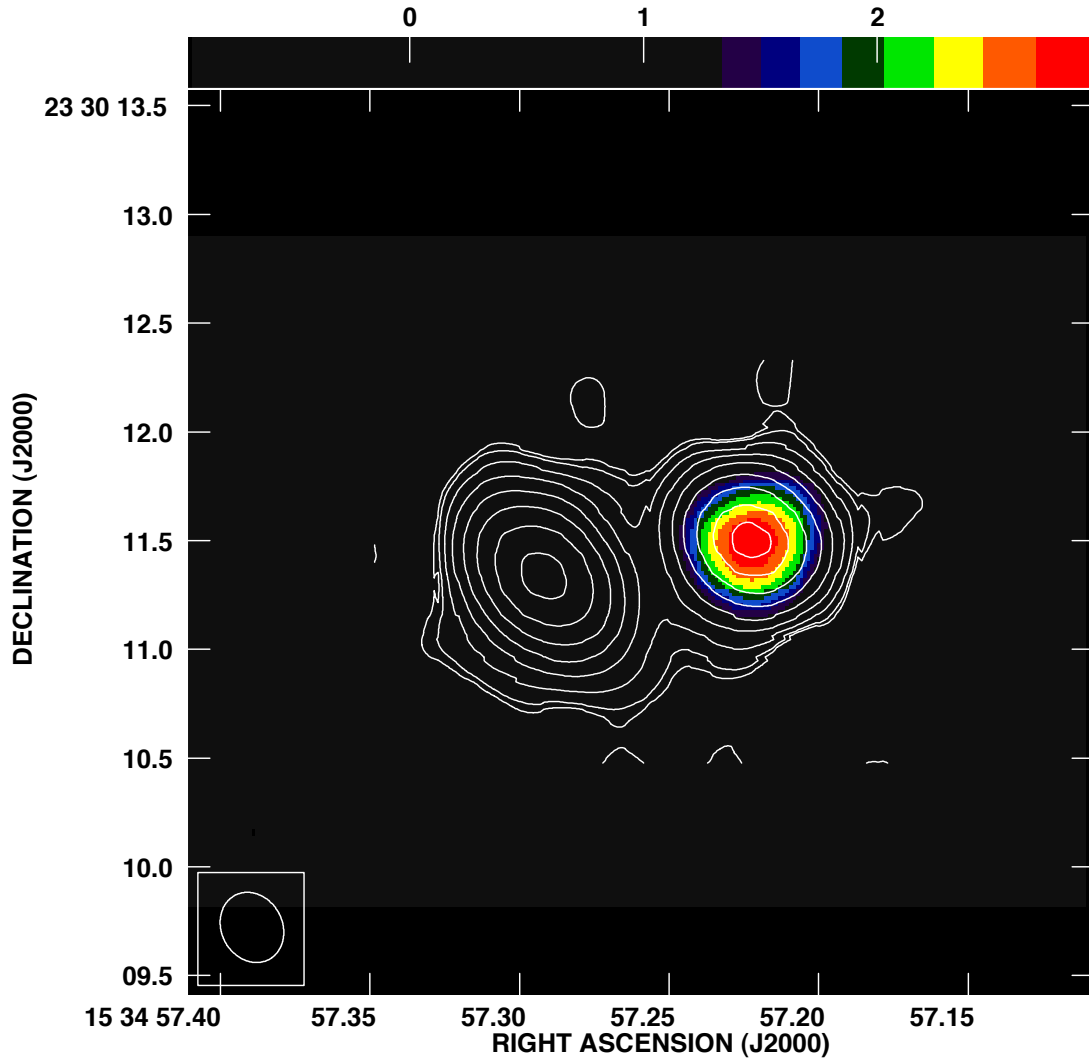
Figure 3.2: Image of the frequency channel in the H$_2$CNH spectral line cube containing the highest peak overlaid on a contour map of the 6.6 GHz continuum. The rectangular box above the image gives the flux densities corresponding to the colors shown in the image in mJy/beam. The RMS for the 6.6 GHz continuum image is 0.23 mJy/beam. The contour levels are $(2, 3, 6, 12, 24, 48, 96, 192, 300) \times$ RMS, and correspond to the 6.6 GHz continuum. In the lower left corner is a representation of the synthesized beam size $(0.4020(1)'' \times 0.3409(8)'')$ for the H$_2$CNH observations. It can be seen that the H$_2$CNH transition occurs solely toward the western nucleus.
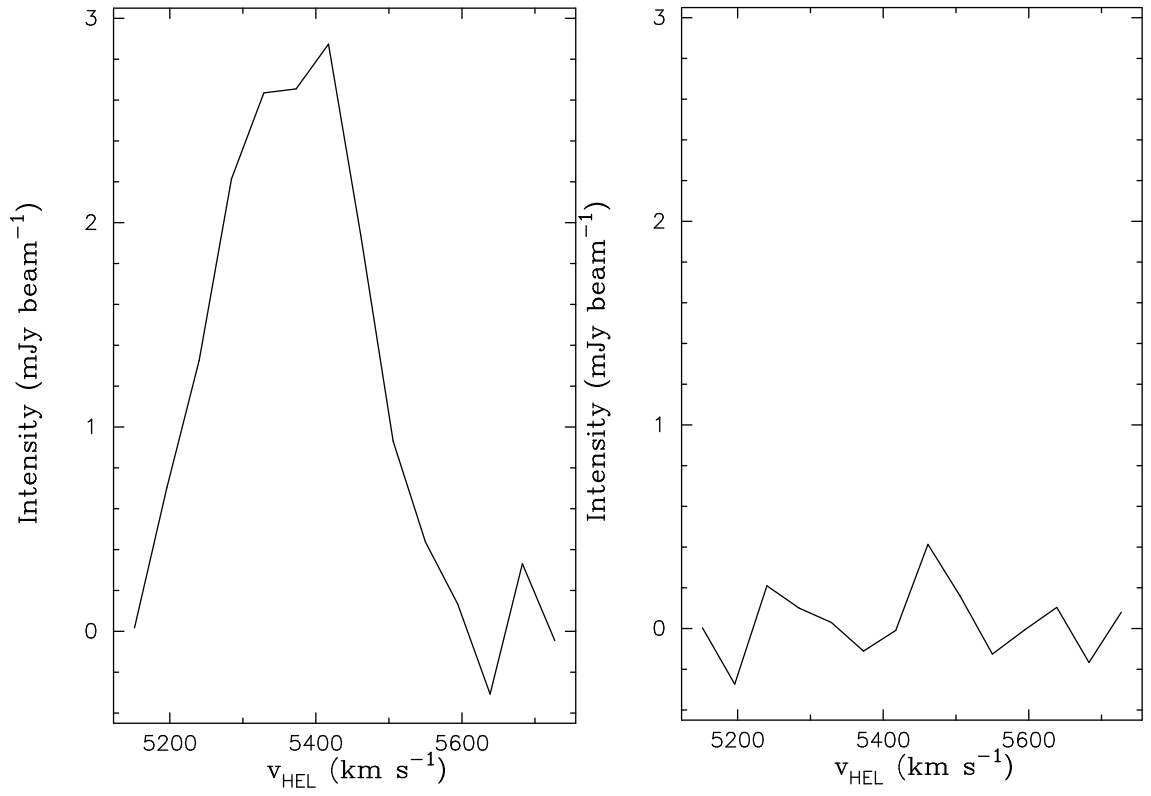
Figure 3.3: Left: Spectrum of H_2CNH toward the western nucleus. Right: Spectrum of H_2CNH toward the eastern nucleus. It is evident that there is only a detection toward the western nucleus.

$$T_b = \frac{c^2 S}{2k\nu^2\Omega},$$ (3.1)

where S is the source flux density, ν is the frequency, and Ω is the solid angle of the source. From the H_2CNH spectral lines it was possible to calculate the corresponding brightness temperature. From Figure 3.2, it can be seen that the angular size of the H_2CNH source in the western nucleus is about the same as the synthesized beam, indicating that the H_2CNH emitting source is either unresolved, or marginally resolved. Using *JMFIT*, we were able to deconvolve the beam from the source, which allowed us to determine the size of the H_2CNH source in the western nucleus to be $(0.25'' \times 0.19'') \pm 0.04''$. Using task *IMSTAT* the flux density was measured to be 3.5 ± 0.1 mJy[1]. Substituting these values into Equation 3.1 then gives a minimum brightness temperature of the H_2CNH emission of 3600 K. This is a *minimum* value for the brightness temperature because we would obtain an even larger value for T_b if future observations at higher resolution determined the size of the H_2CNH emitting region to be smaller than what we observed.

Our calculated brightness temperature can be compared to the value calculated by Salter et al. (2008). These authors used the flux density from their Arecibo observations, but chose to use the size of the source measured by Baan & Haschick (1995) in formaldehyde emission with the VLA in A configuration (equal to $0.27'' \times 0.21''$). They determined a minimum brightness temperature of 2800 K for the H_2CNH line toward Arp 220. Our value is roughly in agreement with their value, and is marginally higher because we have localized the H_2CNH emission to the western nucleus, and have therefore used a smaller source size in Equation 3.1.

Calculations of the brightness temperature can often provide insight into the physical mechanism of the emission. In our case, this calculated minimum brightness temperature of 3600 K is strong evidence that the H_2CNH emission detected is from a maser. As the decomposition temperature of H_2CNH is 1300 K (Nguyen et al. 1996) it is not possible for this to be a thermal emission, as the H_2CNH would have decomposed long before being able to reach a temperature of 3600 K. Therefore the

---

[1] $1\mathrm{Jy} = 10^{-26} \frac{\mathrm{W}}{\mathrm{m}^2\mathrm{Hz}}$

most likely explanation is stimulated emission from a maser. This would make the H_2CNH emission the first ever observed H_2CNH maser (including both galactic and extragalactic observations). The isotropic luminosity of this maser could then be derived from:

$$F = \frac{L}{4\pi r^2},$$ (3.2)

where F is the flux density, L is the luminosity and r is the distance to the object. The flux density of the H_2CNH emission can be measured from the channel map (Figure 3.2) by integrating over the region where the H_2CNH emission is present. This was done using the AIPS task *TVSTAT*, and found to be 3.5 mJy. Using 1 Jy $= 10^{-26}$ W m^{-2} Hz^{-1}, we obtained $F = 3.1 \times 10^{-23}$ W m^{-2} Hz^{-1}. Using the distance to Arp 220 of 77 Mpc (1 Mpc $\equiv 3.1 \times 10^{22}$ m), we obtained a luminosity for the H_2CNH maser of $L = 2.0 \times 10^{27}$ W, that is, $L = 5L_\odot$. Since this is the first H_2CNH maser of its kind, it is very difficult to get a sense at this time of what this luminosity might imply. The best we can do is to compare it to the isotropic luminosities of H_2O masers in a variety of environments, since H_2O masers are one of the most well studied maser phenomena, both in our Galaxy and in external galaxies. In our own Galaxy, the isotropic luminosity of all H_2O masers is $L_{H_2O} \lesssim 10^{-2}\ L_\odot$, except for the H_2O maser in W49 N, which has occasionally flared to $L_{H_2O} \sim 1L_\odot$ (Liljeström & Gwinn 2000). In external galaxies, H_2O maser emission is usually comprised of two types: there are the H_2O megamasers with $L_{H_2O} > 10L_\odot$ (Braatz et al. 1994), with some reaching incredibly high values of up to 23×10^3 L$_\odot$ (Barvainis & Antonucci 2005). There are also the H_2O kilomasers, with $L_{H_2O} < 10L_\odot$ (Tarchi et al. 2009). It is now known that the H_2O megamasers are exclusively powered by activity in Active Galactic Nuclei (AGN), whereas H_2O kilomasers are related primarily to regions of active star formation offset from the nucleus of their parent galaxies, but some fraction of their population could be related to AGN and constitute the low luminosity tail of megamasers (Tarchi et al. 2011). Recently, Brogan et al. (2010) observed several H_2O kilomasers in 3 masing regions toward the Antenna galaxies (NGC 4038/NGC 4039; Arp 244), which are an example of two galaxies in the

process of merging, in which the collision has created several active regions of star formation. These H_2O kilomasers have isotropic luminosities in the range 1.3 to 7.7 $L_\odot$, and all three masing regions were found to be coincident with natal super star clusters containing the equivalent of a few thousand O stars. The isotropic luminosity of the H_2CNH maser from our observations ($L = 5L_\odot$) certainly falls in the same range of luminosities as the H_2O kilomasers, although this coincidence may not mean much, as no H_2O kilomasers have been detected in Arp 220. However, it is interesting that the western nucleus toward which we have observed the H_2CNH emission is undergoing an intense starburst, as we will discuss in more detail in Section 3.3.4 below. Also of interest is the 4.8 GHz transition of formaldehyde (H_2CO) emission toward Arp 220, which was observed by Baan et al. (1986) to be a maser; we note that they observed with the Effelsberg single dish and so would not have had the resolution to decide whether the emission was from one or both nuclei. Its luminosity of 12 $L_\odot$ is very similar to that of our detected H_2CNH maser (5 $L_\odot$). Baan et al. (1986) concluded that the H_2CO maser is being caused by inverted level populations in the foreground gas of Arp 220 amplifying the radio continuum emission from the nucleus. The scenario is likely similar for our H_2CNH maser, especially since we know that we have a column of molecular gas detected in HCN absorption in front of the western nucleus (Section 3.3.4).

3.3 HCN

The J = 5 direct l-type transition in the vibrationally excited state $\nu_2 = 1$ of HCN (Section 1.4.2) was observed in absorption toward Arp 220. In Section 3.3.1, we present the results of these observations by looking at the channel map and the observed spectral line absorption profile. We use the parameters of the observed absorption line and the continuum values to define and measure a quantity called the optical depth in Section 3.3.2, and then find the column density of the HCN absorbing gas in Section 3.3.3. Finally, in Section 3.3.4, we discuss what the HCN observations reveal about the physical conditions in the western nucleus.

3.3.1 Spectral Line Absorption

Figure 3.4 shows a map of HCN absorption toward the two nuclei of Arp 220, which was obtained by plotting the frequency channel with the greatest absorption as described in Section 2.3.1. Figure 3.5 shows the HCN spectra toward the two nuclei of Arp 220. Again, in both figures it is clear that absorption is detected solely toward the western nucleus. In Figure 3.4, absorption is visible solely toward the western nucleus, although as the size of the HCN absorption is about the same as the beam size, it is possible that the HCN absorption is unresolved and in fact smaller than it appears in the figure. In Figure 3.5 the line trough is -3.4 mJy/beam, with a RMS of 0.5 mJy/beam. This gives about a 7 σ detection. Meanwhile there is no trough toward the eastern nucleus that is above the RMS value, signifying a non-detection toward the eastern nucleus. This localization of the HCN absorption to the western nucleus is a new result based solely on the observations reported in this work.

3.3.2 Optical Depth

The optical depth is a dimensionless quantity that measures the amount of radiation that is lost through scattering and absorption as it passes through a medium. It is generally found from the expression:

$$I/I_0 = e^{-\tau}, \tag{3.3}$$

where I_0 is the incident intensity on the medium, I is the intensity after passing through the medium (and therefore this is the observed intensity), and (τ) is the optical depth (Kitchin 1987). For spectral lines observed in absorption, Equation 3.3 can be written in the form:

$$\tau_{peak} = -\ln\left(1 - \frac{S_L}{S_C}\right), \tag{3.4}$$

where S_L refers to the peak flux of the spectral line, whereas S_C is the continuum flux, and τ_{peak} is now the peak optical depth. Note that in order for the natural log to be calculated, one must have $|S_C| \geq |S_L|$, which may appear contrary to what
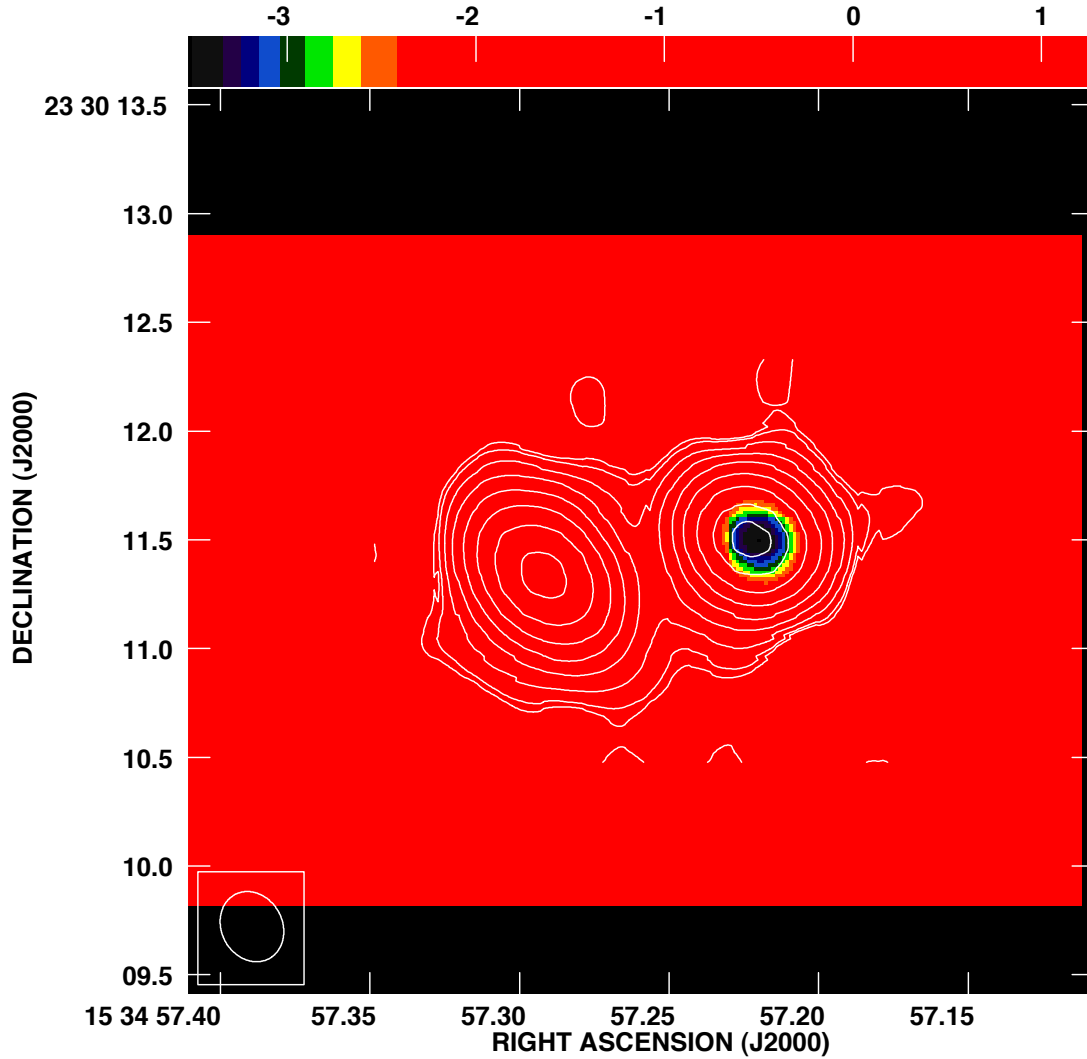
Figure 3.4: Image of the frequency channel in the HCN spectral line cube with the deepest absorption overlaid on a contour plot of the 6.6 GHz continuum. The rectangular box above the image gives the flux densities corresponding to the colors shown in the image in mJy/beam. The negative values represent absorption. The RMS for the 6.6 GHz continuum image is 0.23 mJy/beam. The contour levels are $(2, 3, 6, 12, 24, 48, 96, 192, 300) \times$ RMS. In the lower left corner is a representation of the synthesized beam size of $0.3333(6)'' \times 0.2801(0)''$. Note that the size of the HCN absorbing region is about the same as the synthesized beam size. This means that the HCN absorbing source may be unresolved, in which case it could have dimensions smaller than what is seen in this figure. It can be seen that the HCN transition occurs solely toward the western nucleus.

Figure 3.5: Left: Spectrum of HCN in absorption toward the western nucleus. Right: Spectrum of HCN toward the eastern nucleus. The absorption is detected solely toward the western nucleus.

is seen in Figure 3.5, but it is not. This is because the figure shows the spectral line after the continuum has been subtracted, as described in Section 2.3. In reality, the background continuum is measured at some positive value, and th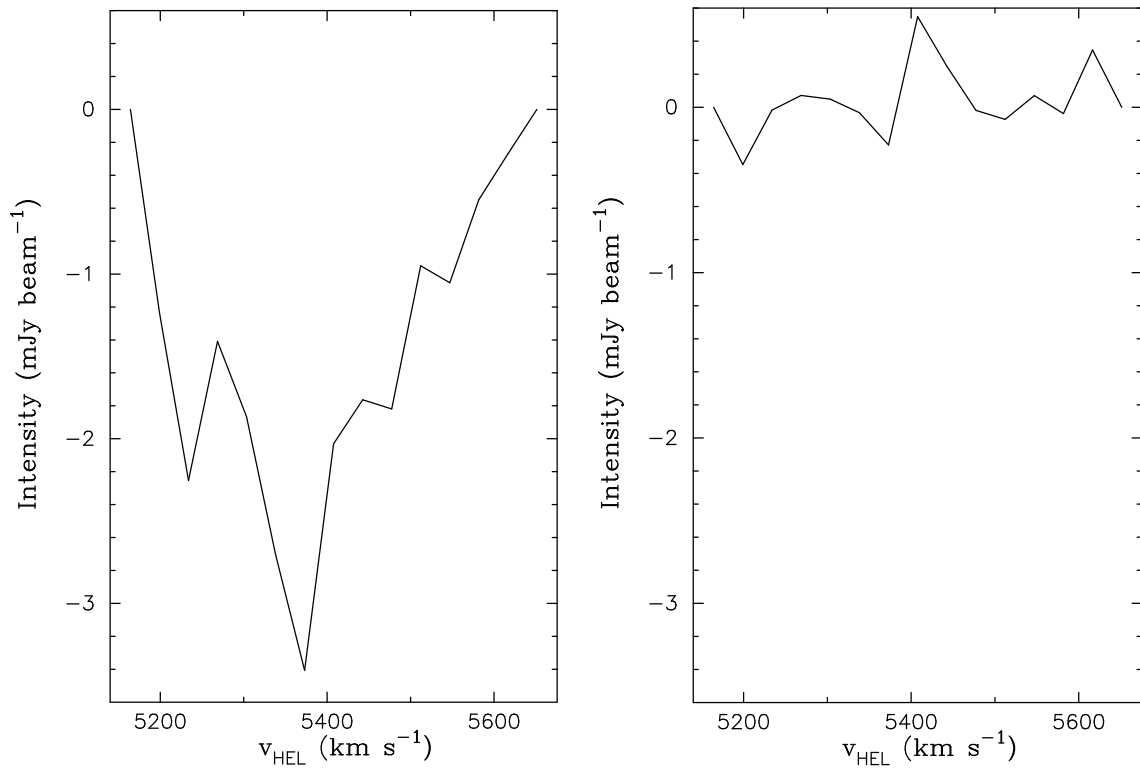e absorption line is seen as a drop in the continuum value. From our data we determined that the ratio of S_L to S_C is $0.0293 \pm .0006$. Substituting these values into Equation 3.4, the optical depth was calculated to be 0.0298 ± 0.0008. This is slightly larger than the optical depth of 0.0205 ± 0.001 calculated from the Arecibo Survey (Salter et al. 2008). This lower value for τ from the Arecibo observations is likely due to the fact that Arecibo observed a larger continuum that was coming from at least both nuclei, which would cause the measured S_C value to be greater. Substitution of a similar value for S_L with a much larger S_C in Equation 3.4 would then yield a lower value for τ.

3.3.3   Column Density

The column density measures the amount of absorbing material along the line of sight. That is, if we imagine a column of gas along the line of sight of length L in which the absorption is occurring, the column density is given by $N = nL$, where n is the particle density of the gas in cm^{-3}. In order to find the column density (N) of the absorbing HCN gas, we used the following equation:

$$N = \frac{8\pi\nu^2}{c^2} \frac{Q(T_{\text{ex}})}{g_u} \frac{\tau\Delta\nu}{A_{ul}} \left[\frac{e^{E_u/kT\text{ex}}}{e^{h\nu/kT_{\text{ex}}} - 1} \right] \tag{3.5}$$

where ν is the rest frequency of the transition, Q is the partition function, g_u is the degeneracy of the upper state equal to $(2J + 1)$, A_{ul} is the Einstein A-coefficient, E_u is the energy of the upper level of the transition, and T_{ex} is the excitation temperature. Equation 3.5 was obtained by combining equations (1) and (2) of Rolffs et al. (2011) and rearranging the combined equation to bring N to the left hand side. The quantities τ and $\Delta\nu$ in these equations are actually drawn from the integral $\int \tau\Delta\nu$. In their calculation for the HCN column density in Galactic clouds, Rolffs et al. (2011) chose to measure the value of this integral by using the

peak optical depth (τ) and the linewidth of their observed absorption lines. In other words, they assumed a gaussian profile; therefore, they had an additional factor of 0.94 in their equation that is not written in Equation 3.5. In our case, since we have measurements over a finite number of channels each with a set channel width, we will calculate the integral by using:

$$\int \tau \Delta \nu = \sum_i \tau_i \, \Delta \nu_i \qquad (3.6)$$

where τ_i is the optical depth in the ith frequency channel, and $\Delta \nu_i$ is the frequency resolution of the observations. The frequency resolution of our HCN observations was 781.25 kHz; thus $\Delta \nu_i$ is a constant that can be moved outside the summation in Equation 3.6. The value of $\sum_i \tau_i$ was determined as per the steps described in Section 2.3.2, and found to be equal to 0.11924. These are the values of τ and $\Delta \nu$ that we will use in Equation 3.5.

Table 3.1 lists the values of all the quantities in Equation 3.5 that we used to calculate the column density N. The value of the rest frequency ν for the HCN $\nu_2 = 1, J = 5$ direct l-type transition was obtained from the Cologne Database of Molecular Spectroscopy (CDMS)[2], while the values of A_{ul} and E_u were obtained from the online spectral line catalog *Splatalogue*[3]; we chose to use the JPL values (referenced within *Splatalogue*). The values of the partition function $Q(T)$ were also obtained from this catalog, except that $Q(T)$ is only listed at a few finite temperatures. Therefore, we plotted these tabulated values of Q, fit a straight line to the plot, and obtained the slope and intercept of the fitted line in order to predict $Q(T)$ at any given temperature. In other words, we calculated the value of the partition function at any given temperature by finding $Q = s\, T_{\text{ex}} + y$. The slope ($s$) and y-intercept (y) are given in Table 3.1. Such a linear interpolation is somewhat crude, but will suffice for this work. A more accurate method would involve interpolating between a larger sample of values tabulated in Barber et al. (2002).

---

[2]http://www.astro.uni-koeln.de/cgi-bin/cdmssearch
[3]http://www.splatalogue.net

Table 3.1: Values of quantities used to determine column density N

Quantity	Symbol	Value
Rest frequency of the $\nu_2 = 1, J = 5$ direct l-type HCN transition[a]	ν	6731.9105×10^6 Hz
Frequency resolution	$\Delta\nu$	7.8125×10^5 Hz[d]
	$\sum \tau_i$	0.11924[d]
Energy of upper state[b]	E_u/k	1088.48986 K
Degeneracy of upper state[c]	g_u	11
Einstein A-coefficient of upper state[b]	A_{ul}	$10^{-8.48362}$
Partition Function $Q(T_{\mathrm{ex}}) = s\,T_{ex} + y$	s	0.46938108[e]
	y	0.55582846[e]
Speed of light	c	3×10^{10} cm s^{-1}
Planck's constant	h	6.624×10^{-34} J.s
Boltzmann constant	k	1.38×10^{-23} J K^{-1}

[a] The value of ν for the HCN transition observed in this work was taken from the Cologne Database of Molecular Spectroscopy (CDMS) at http://www.astro.uni-koeln.de/cgi-bin/cdmssearch.

[b] The values of A_{ul} and E_u were taken from the online spectral line catalog *Splatalogue* at http://www.splatalogue.net. We chose to use the JPL values (referenced within *Splatalogue*).

[c] The degeneracy of the upper state was calculated using $g_u = 2J + 1$, with $J = 5$.

[d] The values of $\Delta\nu$ and $\sum \tau_i$ were taken from our observations.

[e] The partition function values were taken from *Splatalogue* (see note b above) at seven different temperatures: $Q(9K) = 4.757$, $Q(18K) = 9.158$, $Q(37K) = 17.971$, $Q(75K) = 35.602$, $Q(150K) = 70.873$, $Q(225K) = 106.164$, and $Q(300K) = 141.442$, and plotted. A linear fit was made to the plot, and the slope (s) and intercept (y) of this fitted line obtained in order to predict $Q(T)$ at any given temperature.

Using Equation 3.5 and the values listed in Table 3.1, we calculated the HCN column densities N for T_{ex} ranging from 50 K to 1000 K. The plot showed that as T_{ex} increases, N decreases to a minimum value, and then begins to increase again. Figure 3.6 shows this dependence, but is plotted for a restricted range of T_{ex} between 300 K and 700 K to highlight the change in N around the minimum value. We adopt this minimum value of $N = 1.04 \times 10^{19}$ cm^{-2} as the lower limit on the column density of HCN toward the western nucleus of Arp 220. The value of $T_{\mathrm{ex}} = 550$ K corresponding to this minimum value of N is somewhat high, but matches closely with the value of 560 K used by Thorwirth et al. (2003) in their observations of the $J = 8$ through $J = 14$ direct l-type transitions in the $\nu_2 = 1$ vibrational state of HCN toward the proto-planetary nebula CRL 618 in our Galaxy. If, however, the excitation temperature for the $J = 5$ HCN transition is as low as 150 K, as determined by Salter et al. (2008) from the $J = 4$ and $J = 6$ direct l-type transitions of $\nu_2 = 1$ HCN toward Arp 220, then the column density toward the western nucleus would be greater by an order of magnitude ($\sim 10^{20}$ cm^{-2}).

To get a physical understanding of our derived value of the HCN column density, we must convert it to the column density of molecular hydrogen. If we assume that the abundance of HCN in Arp 220 is similar to abundances in our Galaxy, that is $N_{\mathrm{HCN}}/N_{H_2} \sim 10^{-5}$ (Rolffs et al. 2011; Cernicharo et al. 2011), then our lower limit on the HCN column density sets the lower limit on the column density of molecular hydrogen toward the western nucleus in Arp 220 to be $N_{H_2} \approx 1 \times 10^{24}$ cm^{-2}. Meanwhile, if the HCN column density is higher by an order of magnitude due to a lower $T_{\mathrm{ex}} = 150$ K, as discussed above, then the column density of molecular hydrogen would be $\sim 10^{25}$ cm^{-2}. This is in reasonable agreement with values in the literature. Wiedner et al. (2002) derived a lower limit of 9×10^{24} cm^{-2} for $N(H_2)$ toward the western nucleus of Arp 220 based on 342 GHz continuum observations, whereas Martín et al. (2011) set a lower limit of 2.5×10^{23} cm^{-2} from C$_{18}$O observations. If the molecular gas has density $n \sim 10^4$ cm^{-3}, then column densities of 10^{24-25} cm^{-2} would correspond to lengths of the absorbing column of gas along the line of sight of 30-300 pc respectively.
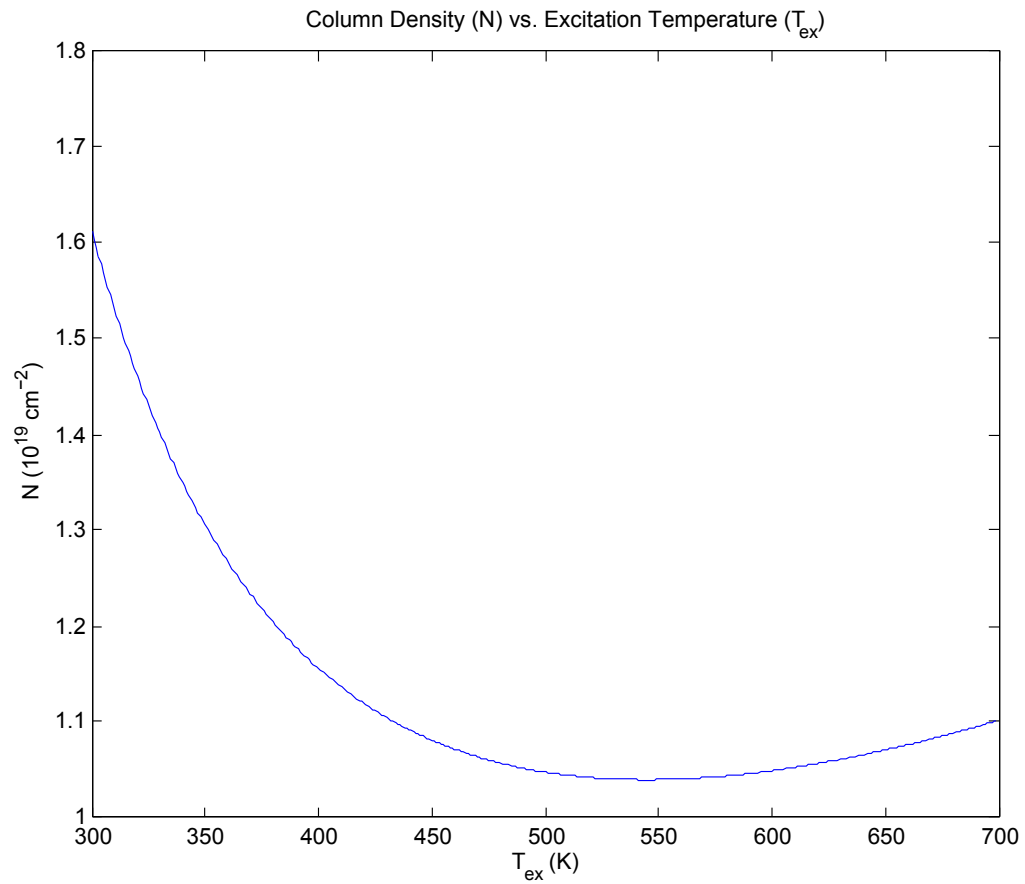
Figure 3.6: Graph showing the dependence of the column density N on the excitation temperature T_{ex} in Equation 3.5. Between 50 K and 1000 K, the column density decreases to a minimum value, then rises again. Only a restricted range of T_{ex} between 300 K to 700 K is shown on this plot to visually emphasize the change around the minimum value.

3.3.4 Discussion of HCN Observations

Our observations have conclusively established that the J $= 5$ direct l-type transition in the vibrationally excited $\nu_2 = 1$ state that we observed in absorption is localized solely toward the western nucleus of Arp 220. Additionally, this absorption line lies about 1090 K above the HCN ground state (Figure 1.14). This leads us to conclude that there must be a column of highly excited molecular gas in the foreground toward the western nucleus, but not toward the eastern nucleus.

Our conclusion is well supported by previous observations. Aalto et al. (2002) observed CN and HC$_3$N emission toward Arp 220, and found that most of the CN emission was from the western nucleus, whereas most of the HC$_3$N emission was from the eastern nucleus. Since CN emission arises mostly in photon dominated regions (PDRs), which are the interfaces between ionized hydrogen (HII) regions and molecular clouds, Aalto et al. (2002) concluded that a significant part of the interstellar medium (ISM) in the western nucleus is located within PDRs. Therefore the ISM in the western nucleus is being strongly affected by an intense UV radiation field, as it is the strong UV radiation from O stars that usually creates such PDRs. Such an intense UV field would also cause the photodissociation of complex molecules like HC$_3$N, which would account for the faintness of the HC$_3$N emission from the western nucleus. Meanwhile, Weidner et al. (2002) found that the ratio of the rotationally excited HCN ($J = 4 - 3$) line to the CO ($J = 3 - 2$) line is larger toward the eastern nucleus. Such rotational lines of HCN are known to trace high density gas ($n \geq 10^4$ cm^{-3}, Gao & Solomon 2004). Weidner et al. (2002) concluded that the eastern nucleus contains higher density gas than the western nucleus. Together, the results of Aalto et al. (2002) and Weidner et al. (2002) are consistent with the claim that the western nucleus is undergoing an intense starburst which has dispersed the dense gas, whereas the eastern nucleus has a substantial amount of dense molecular material (Downes & Solomon 1998). Such intense star formation in the western nucleus also accounts for the presence of the highly excited HCN in which we are observing the absorption. This is because the dominant mode

of populating these vibrationally excited states is likely the radiative pumping by 14 μm infrared photons that come from the dust continuum emission in Arp 220 (Rangwala et al. 2011). This is different from the collisional excitations that are responsible for the low J rotational lines in the ground vibrational state like the HCN ($J = 4-3$) lines observed by Weidner et al. (2002) that need a critical density $\geq 10^4$ cm^{-3}. Radiatively pumped lines, however, are not constrained by the density, and can occur in regions of lower density. Therefore the scenario of an intense starburst in the western nucleus that has dispersed the dense gas (Downes & Solomon 1998) is compatible with the presence of highly excited molecular gas responsible for the HCN absorption that we have observed; the molecules in this foreground gas are shielded from the intense UV radiation of the newly formed stars by the dust, copious amounts of which are present in both nuclei (Greve et al. 2009). In turn, this heated dust in the western nucleus would produce the 14 μm infrared photons that radiatively excite the HCN in the foreground molecular material. Support for this scenario comes from the far-infrared observations (190-670 μm) carried out with the Herschel Space Telescope (Rangwala et al. 2011). Rangwala et al. (2011) observed the high J transitions of HCN in the ground vibrational state; these high J states are also populated by infrared pumping with 14 μm photons. They found that all these high J states appeared in absorption (although they would not have had the angular resolution to localize it to the western nucleus; Arp 220 is a point source at the Herschel resolution). To constrain better the properties of the foreground molecular gas, we need to observe more lines in the vibrationally excited $\nu_2 = 1$ state. Such suggestions for future work are discussed in more detail in Chapter 4.

CHAPTER 4

Conclusions

This chapter summarizes the results and presents the conclusions that can be drawn from the observations of H_2CNH and HCN toward Arp 220 in Section 4.1. Section 4.2 contains a discussion of future work motivated, in part, by the observations reported in this thesis.

4.1 Conclusions

This thesis reported on observations of the 5289.8 MHz $1_{10} - 1_{11}$ spectral line of H_2CNH and the 6731.9 MHz $J = 5$ direct l-type transition in the $\nu_2 = 1$ excited vibrational state of HCN toward Arp 220, the nearest ULIRG. The 5289.8 MHz H_2CNH line was observed in emission toward the western nucleus of Arp 220, but was not detected toward the eastern nucleus. This is a new result from these observations. Consideration of the brightness temperature revealed that the detected H_2CNH emission line is a maser. The likelihood of the emission being a maser was reported in the Arecibo study by Salter et al. (2008), so our observations represent the first independent confirmation of the only H_2CNH maser ever detected. This maser was found to have an isotropic luminosity of 5 $L_\odot$ in our data. This is close to the isotropic luminosity (12 $L_\odot$) of an H_2CO (formaldehyde) maser that was detected in Arp 220 by Baan et al. (1986). Its isotropic luminosity also places it in the same ranks as the H_2O kilomasers that have been detected in other galaxies, most of which are believed to originate from active star forming sites although some are believed to be the low luminosity tail of the H_2O megamasers caused by AGN. The HCN absorption data have revealed the presence of highly excited molecular gas in the foreground of the western nucleus, as discussed below. It seems most likely, therefore, that the H_2CNH maser is being amplified in the foreground gas by the

background continuum of the nucleus.

The 6731.9 MHz HCN line ($\nu_2 = 1, \Delta J = 0, J = 5$) was also observed only toward the western nucleus of Arp 220, but in absorption. No HCN absorption (or emission) was observed toward the eastern nucleus. Once again, this is a new result from these observations. The optical depth of the HCN absorption was found to be 0.0298 ± 0.0008, and the absorbing HCN gas was determined to have a column density of 1.04×10^{19} cm^{-2} corresponding to an excitation temperature near 550 K, although the column density may be higher by an order of magnitude ($\sim 10^{20}$ cm^{-2}) if the excitation temperature were as low as 150 K. Assuming a similar HCN abundance relative to molecular hydrogen as in our Galaxy (10^{-5}), this gives a column density of molecular hydrogen of about 1×10^{24} cm^{-2} (or as much as 10^{25} cm^{-2}), which is in reasonable agreement with the column of molecular hydrogen toward the western nucleus reported by other observers. The observed absorption is likely taking place in a column of highly excited molecular gas in the foreground of the western nucleus. This conclusion is well supported by previous observations that found the western nucleus is undergoing an intense starburst. The intense radiation of the newly formed O stars from this starburst heats the dust around the western nucleus, which produces 14 μm infrared photons that radiatively excite the HCN in the foreground of the western nucleus into its $\nu_2 = 1$ vibrational state.

Together, the observations reported in this thesis provide a self consistent picture of highly excited molecular gas in the foreground of the western nucleus, along with a clear indication that the line of sight toward the western nucleus has different physical conditions compared to the line of sight toward the eastern nucleus. Moreover, this work has also demonstrated some of the new capabilities of the EVLA. This work successfully observed two separate frequencies of 5196 MHz and 6612 MHz. These were the first science observations made by the EVLA that were tuned to two different frequencies in the C-band separated by over 1400 MHz, and have provided a glimpse of what the full EVLA with WIDAR correlator will enable. Even more important, this thesis has demonstrated that the conventional wisdom of observing dense gas with mm-wavelength radio telescopes is not enough. Rotationally excited

mm-wavelength HCN lines have been used extensively in the past to trace dense gas in galaxies. Yet, these lines are found in emission toward both the western and eastern nuclei with column densities of a factor of 100 lower than the ones derived from our observations of vibrationally excited HCN. Clearly, the rotational lines of HCN fail to capture all the important aspects of the dense gas. The EVLA will have an important role to play in understanding the physical conditions of ULIRGs.

4.2   Future Work

Future work in this area falls into two major categories, namely, more extensive observations of Arp 220 itself, and observations of other ULIRGs, especially those that contain dynamic extended structures like the dual nuclei of Arp 220. An EVLA proposal is already in place (AM 1075; PI E. Momjian; time awarded) to observe the $J = 3, 4, 5$ direct l-type transitions in the $\nu_2 = 1$ vibrational state of HCN toward Arp 220 to obtain a better understanding of the highly excited dense molecular gas, and observe simultaneously the H_2CNH and formaldehyde masers to obtain a better understanding of the masing conditions. These observations will exploit the wider bandwith and higher spectral resolution of the upgraded EVLA and its WIDAR correlator. When the EVLA is fully capable of observing continuously up to 50 GHz, transitions up to $J = 14$ should be observable, which will allow for an even more extensive study of the excitation conditions of HCN. A key question would be whether all this HCN is enhanced by starbursts, or whether strong shocks and X-ray radiation have a contribution and if so, by how much. This would yield insight into the powering sources of ULIRGs like Arp 220, that is, whether they are powered by star formation or AGN. Observations of several different transitions (e.g., HCN, CH, HCO^+) with the spatial resolution required to localize them to the western or eastern nucleus of Arp 220 would provide a wealth of information on the difference in the physical and chemical conditions in the two nuclei. Finally, detection of these transitions in other ULIRGs would provide information on the usefulness of this line as a tracer of extreme molecular environments.

REFERENCES

Aalto, S., Polatidis, A. G., Hüttemeister, S., & Curran, S. J. 2002, Astronomy and Astrophysics, 381, 783

Abragam, A., & Proctor, W. 1958, Physics Review, 109, 1441

Araya, E., Baan, W. A., & Hofner, P. 2004, Astrophysical Journal Supplement Series, 154, 541

Baan, W. A., & Haschick, A. D. 1995, Astrophysical Journal, 454, 745

Baan, W. A., Guesten, R., & Haschick, A. D. 1986, Astrophysical Journal, 305, 830

Baan, W. A., Wood, P. A. D., & Haschick, A. D. 1982, Astrophysical Journal Letters, 260, L49

Barber, R. J., Harris, G. J., & Tennyson, J. 2002, Journal of Chemical Physics, 117, 24

Barvainis, R., & Antonucci, R. 2005, Astrophysical Journal Letters, 628, L89

Braatz, J. A., Wilson, A. S., & Henkel, C. 1994, Astrophysical Journal Letters, 437, L99

Brogan, C., Johnson, K., & Darling, J. 2010, Astrophysical Journal Letters, 716, L51

Brotherton, M. 1964, Masers and Lasers (New York, NY: McGraw-Hill Book Company)

Carroll, B., & Ostlie, D. 1996, An Introduction to Modern Astrophysics (1st ed: Addison-Wesley Publishing Company Inc.)

Carroll, B., & Ostlie D. 2007, An Introduction to Modern Astrophysics (2nd ed: Addison-Wesley Publishing Company Inc.)

Cernicharo, J., Pardo, J. R., González-Alfonso, E., Serabyn, E., Phillips, T. G., Benford, D. J., & Mehringer, D. 1999, Astrophysical Journal Letters, 520, L131

Cernicharo, J., Goicoechea, J. R., Pardo, J. R., & Asensio-Ramos, A. 2006, Astrophysical Journal, 642, 940

Cernicharo, J., Agúndez, M., Kahane, C., Guélin, M., Goicoechea, J. R., Marcelino, N., De Beck, E., & Decin, L. 2011, Astronomy and Astrophysics, 529, L3

Cernicharo, J., Pardo, J. R., & Weiss, A. 2006, Astrophysical Journal Letters, 646, L49

Christian E., & Safi-Harb, S. 1998, Ask an Astrophysicist (NASA)

Christopher, M. H., Scoville, N. Z., Stolovy, S. R., & Yun, M. S. 2005, Astrophysical Journal, 622, 346

Clark, B. G. 1980, Astronomy and Astrophysics, 89, 377

Cole, G., 2009, The Expanded Very Large Array Project: A Radio Telescope to Resolve Cosmic Evolution, NRAO, http://www.aoc.nrao.edu/evla/

Curran, S. J., Aalto, S., & Booth, R. S. 2000, Astronomy and Astrophysics Supplement Series, 141, 193

Darling, J. 2005, Future Directions in High Resolution Astronomy, 340, 216

Diamond, P. J., Norris, R. P., Baan, W. A., & Booth, R. S. 1989, Astrophysical Journal Letters, 340, L49

Dickerson, R. 1978, Scientific American, 74

Downes, D., & Eckart, A. 2007, Astronomy and Astrophysics, 468, L57

Downes, D., & Solomon, P. M. 1998, Astrophysical Journal, 507, 615

Gao, Y., & Solomon, P. M. 2004, Astrophysical Journal Supplement Series, 152, 63

Gary, D. 2011, Radio Astronomy: Lecture#9, New Jersey Institute of Technology, http://web.njit.edu/ gary/728/Lecture9.html

Godfrey, P. D., Brown, R. D., Robinson, B. J., & Sinclair, M. W. 1973, Astrophysical Letters, 13, 119

Goldreich, P., & Kwan, J. 1974, Astrophysical Journal, 191, 93

Greve, T. R., Papadopoulos, P. P., Gao, Y., & Radford, S. J. E. 2009, Astrophysical Journal, 692, 1432

Gusel'nikov, L., Volkova, V., Ivanov, P., Inyushkin, S., Shevelkova, L., Zimmermann, G., Ziegler, U., & Ondruschka, B. 1991, Journal of Analytical and Applied Pyrolysis, 21, 79

Högbom, J. A. 1974, Astronomy and Astrophysics Supplement Series, 15, 417

Ivison, R. J., Dunlop, J. S., Smail, I., Dey, A., Liu, M. C., & Graham, J. R. 2000, Astrophysical Journal, 542, 27

Kitchin, C. 1987, Stars, Nebulae and the Interstellar Medium: Observational Physics and Astrophysics (CRC Press)

Kotz, J., Treichel, P., & Townsend, J. 2009, Chemistry & Chemical Reactivity, 7

Kylafis, N. D., & Norman, C. 1987, Astrophysical Journal, 323, 346

Liljeström, T., & Gwinn, C. R. 2000, Astrophysical Journal, 534, 781

Lonsdale, C. J., Diamond, P. J., Thrall, H., Smith, H. E., & Lonsdale, C. J. 2006, Astrophysical Journal, 647, 185

Martín, S., Mauersberger, R., Martín-Pintado, J., Henkel, C., & García-Burillo, S. 2006, Astrophysical Journal Supplement Series, 164, 450

Martín, S., et al. 2011, Astronomy and Astrophysics, 527, A36

Melia, F. 2007, The Galactic Supermassive Black Hole (Princeton, NJ: Princeton University Press)

Morris, M., Palmer, P., Turner, B. E., & Zuckerman, B. 1974, Astrophysical Journal, 191, 349

Mundell, C. G., Ferruit, P., & Pedlar, A. 2001, Astrophysical Journal, 560, 168

Narvey-Smith, L. 2011, Astrophysical Masers, Institute of Astronomy, University of Sydney, http://www.physics.usyd.edu.au/pdfs/current/tsp/tsp2008/LisaHarveySmith.pdf

NASA, ESA, the Hubble Heritage Team (STScl/AURA)-ESA/Hubble Collaboration & Evans, A. 2008, Arp 220

Nguyen, M., Sengupta, D., & Ha, T. 1996, Journal of Physical Chemistry, 100, 6499

Norris, R. P. 1988, Monthly Notices of the Royal Astronomical Society, 230, 345

NRAO 2008, VLA Art Gallery, NRAO, http://www.vla.nrao.edu/genpub/artgallery/

NRAO 2009, Status of Receiver Upgrades, NRAO, http://www.vla.nrao.edu/astro/guides/evlareturn/receivers/index.shtml

NRAO 2010, Plan for ALMA Early Science Cycle 0, NRAO, http://science.nrao.edu/alma/preannounce-full.shtml

Pandian, J. D., Menten, K. M., & Goldsmith, P. F. 2009, Astrophysical Journal, 706, 1609

Perley, R. 2010, Fundamentals of Radio Interferometry, Twelfth Synthesis Imaging Workshop, NRAO, http://www.aoc.nrao.edu/events/synthesis/2010/lectures10.html

Peterson, B. 1997, An Introduction to Active Galactic Nuclei (Cambridge, UK: Cambridge University Press)

Pihlström, Y. 2010, Spectral Line Observing, Twelfth Synthesis Imaging Workshop, NRAO, http://www.aoc.nrao.edu/events/synthesis/2010/lectures10.html

Qiu, K., Zhang, Q., & Menten, K. M. 2011, Astrophysical Journal, 728, 6

Rangwala, N., et al. 2011, arXiv:1106.5054

Rolffs, R., Schilke, P., Wyrowski, F., Dullemond, C., Menten, K. M., Thorwirth, S., & Belloche, A. 2011, Astronomy and Astrophysics, 529, A76

Rovilos, E., Diamond, P., Lonsdale, C., Lonsdale, C., & Smith, H. 2003, Monthly Notices of the Royal Astronomical Society, 342, 373

Sakamoto, K., Scoville, N. Z., Yun, M. S., Crosas, M., Genzel, R., & Tacconi, L. J. 1999, Astrophysical Journal, 514, 68

Sakamoto, K., Mao, R.-Q., Matsushita, S., Peck, A. B., Sawada, T., & Wiedner, M. C. 2011, Astrophysical Journal, 735, 19

Saleh, B., & Teicj, M. 1991, Fundamentals of Photonics (Manchester, MI: John Wiley and Sons)

Salter, C. J., Ghosh, T., Catinella, B., Lebron, M., Lerner, M. S., Minchin, R., & Momjian, E. 2008, The Astronomical Journal, 136, 389

Scoville, N. Z., Sargent, A. I., Sanders, D. B., & Soifer, B. T. 1991, Astrophysical Journal Letters, 366, L5

Scoville, N. Z., Yun, M. S., & Bryant, P. M. 1997, IAU Symposium, 170, 305

Scoville, N. Z., et al. 1998, Astrophysical Journal Letters, 492, L107

Shulman, R. G., & Townes, C. H. 1950, Phys. Rev., 77, 421

Soifer, B. T., et al. 1984, Astrophysical Journal Letters, 283, L1

Soifer, B. T., Sanders, D. B., Madore, B. F., Neugebauer, G., Danielson, G. E., Elias, J. H., Lonsdale, C. J., & Rice, W. L. 1987, Astrophysical Journal, 320, 238

Solomon, P. M., Downes, D., & Radford, S. J. E. 1992, Astrophysical Journal Letters, 387, L55

Takano, S., Nakanishi, K., Nakai, N., & Takano, T. 2005, Publications of the Astronomical Society of Japan, 57, L29

Tarchi, A., Tingay, S., Surcis, G., & Castangia, P. 2009, ATNF proposal V314, Semester: April, 2009, 2120

Tarchi, A., Castangia, P., Henkel, C., Surcis, G., & Menten, K. M. 2011, Astronomy and Astrophysics, 525, A91

Thorwirth, S., Wyrowski, F., Schilke, P., Menten, K. M., Brünken, S., Müller, H. S. P., & Winnewisser, G. 2003, Astrophysical Journal, 586, 338

Ulvestad, J., Perley, R., & Chandler, C. 2006, The Very Large Array Observational Status, NRAO, http://www.vla.nrao.edu/astro/guides/vlas/current/

Wiedner, M. C., Wilson, C. D., Harrison, A., Hills, R. E., Lay, O. P., & Carlstrom, J. E. 2002, Astrophysical Journal, 581, 229

Wrobel, J., & Walker, R. 2010, in Twelfth Synthesis Imaging Workshop, Sensitivity, ed. G. B. Taylor, C. L. Carilli, R. A. Perley (Socorro, NM: NRAO), 171

Wu, J., Evans, N. J., II, Gao, Y., Solomon, P. M., Shirley, Y. L., & Vanden Bout, P. A. 2005, Astrophysical Journal Letters, 635, L173